Earth and Space Science

RESEARCH ARTICLE
10.1029/2021EA001695

Patched Local Lunar Gravity Solutions Using GRAIL Data

Sander Goossens[1,2,3,4], **Álvaro Fernández Mora**[1,2,3,5,6], **Eduard Heijkoop**[1,2,3,5,7], and **Terence J. Sabaka**[2]

[1]Center for Space Sciences and Technology, University of Maryland, Baltimore, MD, USA, [2]NASA Goddard Space Flight Center, Greenbelt, MD, USA, [3]Center for Research and Exploration in Space Science and Technology (CRESST) II, NASA/GSFC, Greenbelt, MD, USA, [4]Now at Planetary Geology, Geophysics, and Geochemistry Laboratory, NASA Goddard Space Flight Center, Greenbelt, MD, USA, [5]Faculty of Aerospace Engineering, Delft University of Technology, Delft, The Netherlands, [6]Now at Faculty of Mathematics and Computer Science, University of Barcelona, Barcelona, Spain, [7]Now at The Colorado Center for Astrodynamics Research and the Earth Science and Observation Center of the Cooperative Institute for Research in Environmental Sciences at the University of Colorado, Boulder, CO, USA

Key Points:

- We determine 14 local gravity field solutions covering the entire Moon using GRAIL intersatellite range-rate data
- We patch the local solutions into a global map, which shows no seams, minimizing boundary effects
- Our solution has improved correlations between gravity and topography compared to standard global solutions, with less computational effort

Correspondence to:
S. Goossens,
sander.j.goossens@nasa.gov

Citation:
Goossens, S., Fernández Mora, Á., Heijkoop, E., & Sabaka, T. J. (2021). Patched local lunar gravity solutions using GRAIL data. *Earth and Space Science*, *8*, e2021EA001695. https://doi.org/10.1029/2021EA001695

Received 5 FEB 2021
Accepted 3 OCT 2021

Author Contributions:
Conceptualization: Sander Goossens, Álvaro Fernández Mora, Eduard Heijkoop, Terence J. Sabaka
Data curation: Sander Goossens
Formal analysis: Sander Goossens, Álvaro Fernández Mora, Eduard Heijkoop, Terence J. Sabaka
Funding acquisition: Sander Goossens
Investigation: Sander Goossens, Álvaro Fernández Mora, Eduard Heijkoop, Terence J. Sabaka
Methodology: Sander Goossens, Álvaro Fernández Mora, Eduard Heijkoop, Terence J. Sabaka

Abstract We present a method to determine local gravity fields for the Moon using Gravity Recovery and Interior Laboratory (GRAIL) data. We express gravity as gridded gravity anomalies on a sphere, and we estimate adjustments to a background global start model expressed in spherical harmonics. We processed GRAIL Ka-band range-rate data with a short-arc approach, using only data over the area of interest. We determine our gravity solutions using neighbor smoothing constraints. We divided the entire Moon into 12 regions and 2 polar caps, with a resolution of $0.15° \times 0.15°$ (which is equivalent to degree and order 1199 in spherical harmonics), and determined the optimal smoothing parameter for each area by comparing localized correlations between gravity and topography for each solution set. Our selected areas share nodes with surrounding areas and they are overlapping. To mitigate boundary effects, we patch the solutions together by symmetrically omitting the boundary parts of overlapping solutions. Our new solution has been iterated, and it has improved correlations with topography when compared to a fully iterated global model. Our method requires fewer resources, and can easily handle regionally varying resolution or constraints. The smooth model describes small-scale features clearly, and can be used in local studies of the structure of the lunar crust.

Plain Language Summary The gravity field of a planet depends on the density distribution in its interior, and as such, improved knowledge of the gravity field can help in determining the interior structure of the planet. Here, we have analyzed the data from the Gravity Recovery and Interior Laboratory (GRAIL) mission to make local maps of the Moon's gravity field. Standard analysis of GRAIL data has focused on determining global models of the Moon's gravity field, partly because the tools of geophysics that are used to study the Moon's interior make use of such models, which are expressed in what are called spherical harmonics. However, if the data coverage is varying geographically, spherical harmonics are more difficult to determine precisely. We have applied a local method that can more readily handle variations in data coverage. We divided the Moon into 14 separate regions, and determined the optimal solution for each. We evaluated each solution by comparing it with the Moon's topography. GRAIL found that gravity and topography are highly correlated on the Moon, which we will leverage to independently evaluate our solution. We then patched together our separate maps into one global map. Our new model has improved correlations with topography when compared with a standard global model, but it takes fewer computational resources to make. Together with the easy way to handle geographically varying data coverage, this makes our method and model a good alternative to standard models. Our new model is smooth and has a resolution of $0.15° \times 0.15°$ (which is 4.5 km by 4.5 km at the equator) and can be used to study the structure of the Moon's crust at small scales.

1. Introduction

The gravitational field of a planet depends on its internal density distribution, and can thus be used to constrain models of its interior structure. Gravity field models are often expressed in global spherical harmonics because these functions are a solution to Laplace's equation that describes the gravitational potential outside a sphere that encompasses the entire planet (e.g., Heiskanen & Moritz, 1984; Kaula, 1966). In general, models of a planet's gravity field are determined with some combination of radiometric tracking, for

Project Administration: Sander Goossens
Software: Sander Goossens, Álvaro Fernández Mora, Eduard Heijkoop, Terence J. Sabaka
Supervision: Sander Goossens
Validation: Sander Goossens, Álvaro Fernández Mora, Eduard Heijkoop, Terence J. Sabaka
Visualization: Sander Goossens
Writing – original draft: Sander Goossens
Writing – review & editing: Sander Goossens, Álvaro Fernández Mora, Eduard Heijkoop, Terence J. Sabaka

example using the Deep Space Network (DSN) in the case of NASA missions, and other data such as camera and altimetry data. Historically, the determination of the Moon's gravity field has been hampered by the fact that the Earth and Moon are in a 1:1 spin-orbit resonance which means that spacecraft cannot be tracked from Earth when they are over the Moon's farside. Nonetheless, global gravity field models expressed in spherical harmonics have been determined from nearside spacecraft tracking data by applying a constraint that suppresses the power in the solution, which would otherwise be unreasonably large due to the gap in data coverage over the farside (e.g., Floberghagen, 2001; Konopliv et al., 2001; Lemoine et al., 1997). This constraint is called a Kaula law, after the observation that the variance in gravity coefficients follows a power law (Kaula, 1966).

This all changed with two recent lunar missions: the Japanese Selenological and Engineering Explorer (SELENE, also called Kaguya) mission (Kato et al., 2010), and NASA's Gravity and Interior Laboratory (GRAIL) mission (Zuber, Smith, Lehman, et al., 2013). SELENE consisted of three spacecraft in total: a main satellite in a circular lunar orbit, and two subsatellites in elliptical orbits. The mission applied the technique of high-low satellite-to-satellite tracking, where a relay satellite in an elliptical orbit was simultaneously visible from Earth and from the main satellite that was in a lower orbit. By tracking the main satellite while it was over the farside through the relay satellite, SELENE provided the first global lunar gravity measurements (Matsumoto et al., 2010; Namiki et al., 2009). In addition, SELENE's other subsatellite was used to provide Very Long Baseline Interferometry (VLBI) measurements (Kikuchi et al., 2009; Liu et al., 2010) that were also used to further improve the gravity field model (Goossens et al., 2011). The GRAIL mission applied the technique of low-low satellite-to-satellite tracking. It consisted of two identical spacecraft in identical low lunar orbits separated by a relatively short distance. Its single science instrument was a system that measured the changes in the distance between the satellites using precise Ka-band ranging (Asmar et al., 2013; Klipstein et al., 2013). This was a modified version of the system on the Gravity Recovery and Climate Experiment (GRACE) mission (Tapley, Bettadpur, et al., 2004) that mapped the Earth's gravity field. This system provided the basic GRAIL observable, Ka-band Range Rate (KBRR), which is the difference between the spacecraft velocities projected along the line-of-sight vector connecting the two spacecraft. The noise level for KBRR data was reported to be between 0.03 and 0.05 μm/s (Konopliv et al., 2014; Lemoine et al., 2014), see also Section 5.

The GRAIL mission was split into two phases: a Primary Mission (PM) that lasted from March 1, 2012 to May 30, 2012, and an Extended Mission (XM) that lasted from August 1 to December 14, 2012. During the PM the satellites had an average altitude of 50 km above lunar surface, and the distance between the two spacecrafts varied from 80 to 220 km. During the XM, the altitude was lowered, first to about 23 km, and to 11–20 km after November 11, 2012 until the end of the mission. The distance between the spacecraft did not vary as much as during the PM, and was kept to 40–60 km. The GRAIL mission exceeded all its requirements, and has provided the highest resolution gravity field models from spacecraft data only, by virtue of the low altitudes that are possible at the Moon. During its PM, its original requirement of delivering a gravity field model of degree and order 180 in spherical harmonics (which is roughly equal to a spatial resolution of 1° by 1°, or 30 km by 30 km, at the lunar equator) was easily surpassed, with the presentation of a degree and order 420 model (Zuber, Smith, Watkins, et al., 2013). After the PM this was followed by models of degree and order 660 (Konopliv et al., 2013; Lemoine et al., 2013). The low-altitude data from the XM meant that the resolution of the models could be extended even further, up to degree and order 900 (Konopliv et al., 2014; Lemoine et al., 2014). Finally, the most recent models, based on GRAIL data only, have a maximum resolution of degree and order 1,200 (Goossens et al., 2020) or 1,500 (Park et al., 2015).

However, the altitude of the spacecraft above the surface during the GRAIL mission varied considerably, as shown in Figure 1. For the global gravity field models, this means that their effective resolution varies spatially. This is best exemplified by maps of degree strength, which is the degree value where the model has a signal-to-noise ratio of 1. This can be computed from the covariance of the solutions by comparing the anomaly error at a location (for different maximum degrees of the model) with the expected signal from a Kaula law. The degree strength is then the degree at which this error matches the expected signal. This was first used for Venus by Konopliv et al. (1999) and this has proven to be a useful indicator of model resolution. Recent results for global models using GRAIL data show a varying degree strength and thus a varying effective resolution (Goossens et al., 2020; Konopliv et al., 2014; Lemoine et al., 2014). The smoothness

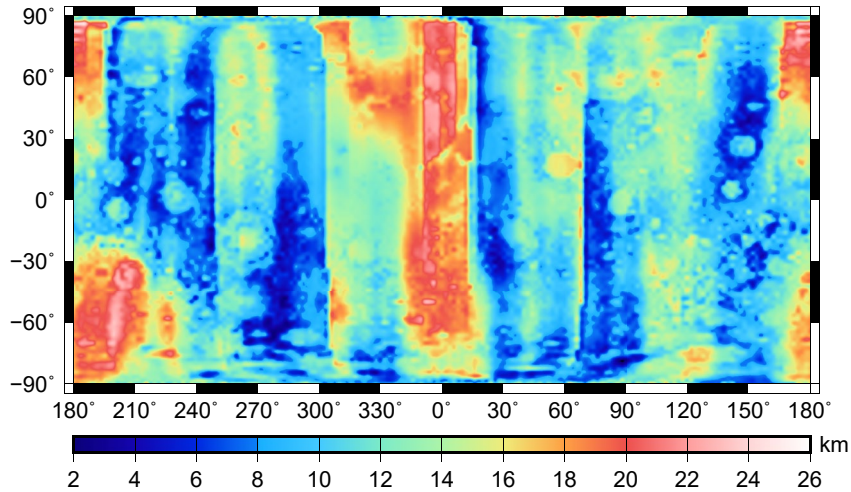

Figure 1. Minimum altitude above topography during the entire Gravity Recovery and Interior Laboratory (GRAIL) mission. Variations in minimum altitude translate into varying sensitivity to small-scale surface features. The map projection is an equidistant cylindrical projection centered on the nearside.

constraints that global models require are often applied spectrally and uniformly, which can lead to an underestimation of peak amplitudes (e.g., Floberghagen, 2002; Konopliv et al., 1999). Global spherical harmonics are thus not optimal when the spatial data coverage is not homogeneous. In such instances, local methods can be advantageous.

In satellite geodesy, local methods have long since been applied to different data types from satellites orbiting various bodies. Some examples include analysis for Venus (e.g., Barriot et al., 1998; Kaula, 1996), Mars (e.g., Beuthe et al., 2006), and Jupiter's moon Ganymede (Anderson et al., 2004; Palguta et al., 2006), without listing the many applications to Earth-orbiting satellites. The determination of the Moon's gravity field was especially suitable for local methods because of the farside gap prior to the GRAIL and SELENE missions. Examples include the discovery of the prominent mass concentrations (mascons) on the nearside of the Moon from the analysis of Doppler residuals from the Lunar Orbiter V spacecraft using a short-arc line-of-sight analysis (Muller & Sjogren, 1968), and recent results using Lunar Prospector or SELENE data (e.g., Goossens et al., 2012; Goossens, Visser, & Ambrosius, 2005; Goossens, Visser, Heki, & Ambrosius, 2005; Han, 2008; Han et al., 2011; Sugano & Heki, 2004a). Local analysis has also been used for estimating lithospheric thickness and addressing isostasy of various craters and basins on the Moon (e.g., Crosby & McKenzie, 2005; Sugano & Heki, 2004b).

GRAIL KBRR data are ideally suited for estimating local parameters: each KBRR measurement is approximately directly proportional to the difference in gravity potential at the two satellite locations, making them well-suited to estimate local parameters (Rowlands et al., 2005). Several analyses have thus used GRAIL data for regional gravity field estimation (e.g., Han, 2013; Han et al., 2014; Šprlák et al., 2020). In Goossens et al. (2014), we utilized this and produced a local map of gravity at the south pole of the Moon using GRAIL extended mission data. That local model improved the data fit, extended the resolution of the background global model, and it improved the correlations with topography, thus showing it is a viable method to extract high-resolution information from the data. Higher correlations between gravity and topography are indicative of an improved gravity model because at small scales (higher spherical harmonic degrees) gravity is expected to closely follow topography (e.g., Wieczorek, 2015). Here, we extend that analysis to cover the entire Moon. We determine 14 separate solutions that cover the Moon, with overlap at the boundaries to mitigate boundary effects. We will show that this results in a seamless map of lunar gravity anomalies, that has improved correlations with topography when compared to a standard analysis using spherical harmonics, at lower computational costs. For lunar topography, we use the results of the Lunar Orbiter Laser Altimeter (LOLA) instrument (Smith, Zuber, Jackson, et al., 2010; Smith, Zuber, Neumann, et al., 2010; Smith et al., 2016) onboard the Lunar Reconnaissance Orbiter (LRO) spacecraft (Chin et al., 2007).

This paper is structured as follows: in Section 2, we will introduce the local gravity representation. We discuss the estimation method, including the constraint used in our analysis, in Section 3. In Section 4, we will discuss the optimal processing of short arcs, and in Section 5, we will discuss determining the optimal solution for each area. We present the method of combination of these maps in Section 6. We will discuss the results in Section 7 and present the conclusions in Section 8.

2. Local Gravity Representation

In our earlier local effort with GRAIL data (Goossens et al., 2014), we represented gravity in terms of gridded gravity anomalies. While many other local representations exist, we again choose anomalies for several reasons. They can easily be connected to global spherical harmonics, which will make comparisons with topography in terms of correlations between the two easier. They are also well-suited for the spatial neighbor constraint that we apply. In addition, they are relatively straightforward to implement and estimate in our processing software. Here, we first introduce the gravity anomaly, and then we discuss the discretization of the anomaly equation and the constraint we apply. In Appendix A, we provide more details about the gravity anomalies, the expressions used to compute the partial derivatives of measurements with respect to the anomalies, and their relationship with respect to spherical harmonics.

2.1. Gravity Anomalies

Following Heiskanen and Moritz (1984), the full gravitational potential W can be expressed as the sum of the normal potential U on a reference surface (e.g., a sphere or ellipsoid), and the disturbing potential T. The geoid is defined as a surface with constant potential, say W_0, and the reference surface can then be chosen with the same potential W_0. The geoid and reference surface will not be the same. A point P on the geoid will have a point Q on the reference surface projected along the normal direction n of the reference surface (see Appendix A for a depiction of the relationship between points P and Q). Normal gravity γ at the reference surface can be defined as $\gamma = -\partial U/\partial n$, and a gravity anomaly Δg is defined as the difference between gravity g_P at point P and normal gravity γ_Q at point Q (Heiskanen & Moritz, 1984; Sjöberg & Bagherbandi, 2017):

$$\Delta g = g_P - \gamma_Q. \tag{1}$$

In spherical approximation (where normal gravity at Q is simply GM/r^2, with GM the gravitational constant times mass, and r the reference sphere radius), this becomes (Heiskanen & Moritz, 1984):

$$\Delta g = -\frac{\partial T}{\partial r} - 2\frac{T}{r}. \tag{2}$$

A gravity anomaly in this sense thus refers to the geoid surface, and is equal to the radial derivative of the disturbing potential, with a correction for the difference in reference surfaces used. This is the definition of gravity anomaly often used in geodesy, and we also apply it here. In geophysics, the radial derivative of the disturbing potential, $-\partial T/\partial r$, is often used, and it is the difference between gravity and normal gravity both at P. In geodesy, this is called the gravity disturbance. There is some confusion about these terms between the disciplines of geodesy and geophysics because of the difference in reference surface used, and what is called a disturbance here would be called an anomaly in geophysics (Hackney & Featherstone, 2003; Li & Götze, 2001). Our anomalies correspond to a spherical reference surface, which has a radius of 1,738 km.

Equation 2 relates the gravity anomaly to the disturbing potential T. Conversely, the disturbing potential T can, of course, also be expressed as a function of the gravity anomaly, and this is what is eventually needed in order to estimate the anomalies. We only repeat the result here as the derivation can be found in, for example, Heiskanen and Moritz (1984):

$$T(P) = \frac{a_e}{4\pi} \iint_{\sigma(Q)} S(P,Q)\, \Delta g(Q)\, d\sigma(Q), \tag{3}$$

where P is the point where the disturbing potential T is to be computed, Q is the point on the reference surface σ_Q, a_e is the reference radius (here, we use a value of 1,738 km), and $S(P, Q)$ is the kernel function in this integral equation (see Appendix A for details).

Finally, because the integral is over the entire surface, and the functions are harmonic outside of the Brillouin sphere (the circumscribing sphere that fits the entire mass of the body), spherical harmonic equivalents exist. Using the standard expression for the potential in spherical harmonics (see Kaula, 1966, and additional explanations in Appendix A) and Equation 2, Δg can be expressed as:

$$\Delta g(r,\lambda,\phi) = \frac{GM}{r^2}\sum_{l=2}^{\infty}(l-1)\left(\frac{a_e}{r}\right)^l \sum_{m=0}^{l}\left(\bar{C}_{lm}\cos(m\lambda)+\bar{S}_{lm}\sin(m\lambda)\right)\bar{P}_{lm}(\sin\phi), \tag{4}$$

where r,λ,ϕ are the spherical coordinates radius, longitude, and latitude, respectively, $\bar{C}_{lm}$ and $\bar{S}_{lm}$ are the normalized harmonic coefficients of the expansion of degree and order m, and $\bar{P}_{lm}$ are the normalized associated Legendre functions. Normalization here is the standard 4π normalization used in geodesy (see Appendix A). In practice, this expansion is evaluated up to a maximum degree, $L_{\max}$. Because of this equivalency, a global anomaly grid can easily be expressed in spherical harmonics. A local grid can also be expressed in spherical harmonics by using spherical harmonic transformations. We will use this frequently, because we can then also apply localized spectral analysis (Wieczorek & Simons, 2005, 2007) to compute correlations between gravity and topography for the selected area only. This will serve as an independent evaluation of the resulting local gravity model. Correlations $\gamma(l)$ per degree between two quantities expressed in spherical harmonics with coefficients $(\bar{C}^A_{lm},\bar{S}^A_{lm})$ and $(\bar{C}^B_{lm},\bar{S}^B_{lm})$ are computed using the cross power $S_{AB}(l)$ following (e.g., Wieczorek, 2015)

$$\begin{aligned} S_{AB}(l) &= \sum_{m=0}^{l}\left(\bar{C}^A_{lm}\bar{C}^B_{lm}+\bar{S}^A_{lm}\bar{S}^B_{lm}\right), \\ \gamma(l) &= \frac{S_{AB}(l)}{\sqrt{S_{AA}(l)S_{BB}(l)}}. \end{aligned} \tag{5}$$

2.2. Discretization

Equation 3 is the basis of our analysis because it expresses the potential as a function of the anomaly. From the potential, the acceleration on the spacecraft can be computed, and this is how, through variational equations (e.g., Montenbruck & Gill, 2000; Tapley, Schutz, & Born, 2004), we can estimate the anomalies from tracking data. See Section 3 for more details. Here, we take the radial derivative of the potential, $\delta_r(P) = \partial T/\partial r$, as an example, and we show results for additional directions in Appendix A. The radial derivative of T expressed as a function of anomalies Δg is:

$$\delta_r(P) = \frac{a_e}{4\pi}\iint_{\sigma(Q)}\frac{\partial S(r,\psi)}{\partial r}\Delta g(Q)\,d\sigma(Q). \tag{6}$$

We discretize the integral equations by replacing the integral with a sum over gridded gravity anomalies. The expression for the radial acceleration would then be:

$$\delta_r(P) = \frac{a_e}{4\pi}\sum_{i=1}^{M}\frac{\partial S(P,Q_i)}{\partial r}\Delta g(Q_i)\,d\sigma(Q_i), \tag{7}$$

where M is the number of anomalies. In this representation, the kernel function would, for example, be evaluated at the midpoint of a grid cell of n by n degrees (although it does not necessarily have to be a regular grid), and $d\sigma(Q_i)$ would be the area of that particular grid cell. The anomaly $\Delta g(Q_i)$ would be the anomaly for the entire grid cell, and in this way, partials with respect to each anomaly can be easily obtained from Equation 7.

In our earlier work, we divided each grid cell into four smaller, equal parts, evaluated the kernel at the center point of each subcell, and computed the contribution of one anomaly in that way. However, this midpoint approach can result in discretization errors, as pointed out by Hirt et al. (2011). Here, instead of discretization by subdivision using the midpoints, we follow Hirt et al. (2011) and compute the integral over each n by n cell using Gauss-Legendre quadrature. For each cell, we determine the Gauss-Legendre nodes (four nodes for each cell, just like we subdivided the cell into four parts before), and then evaluate the analytical

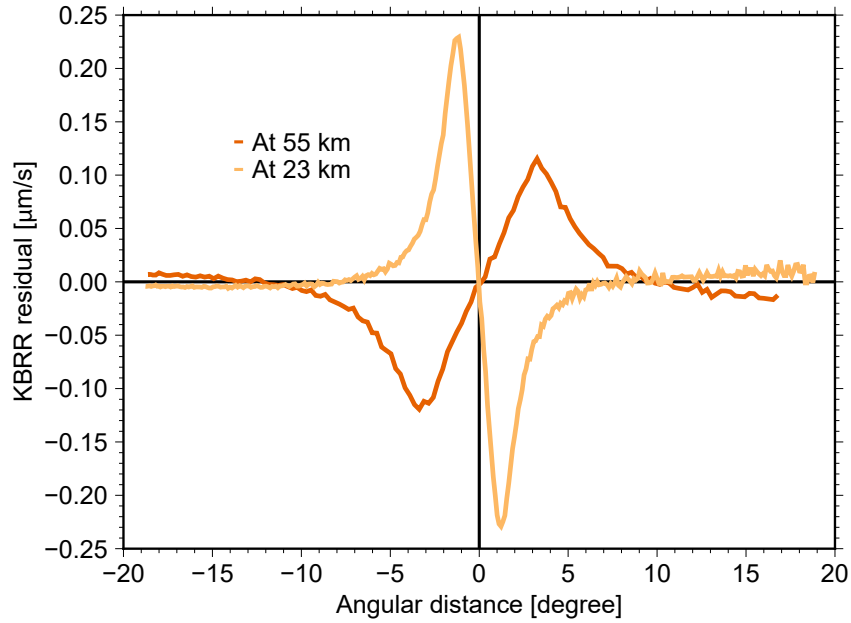

Figure 2. Effect of a l/6° by l/6° anomaly with an amplitude of 1 mGal on GRAIL KBRR data at the PM and XM altitude.

expression for the kernel at that node. This is then multiplied by the quadrature weight, and this is how we integrate the kernel function for each anomaly. We tested using more nodes but that did not change the results. Using this new integration method, we compared solutions for a test area with our earlier midpoint method, and found small improvements, in terms of correlations with topography. We also tested defining the entire grid on Gauss-Legendre node points (each cell would then have only one Gauss-Legendre point, instead of 4), but found a slight degradation for this grid. Finally, for the pole anomaly we define a cap with a radius of n / 2 degrees, and we use 36 nodes for the integration of the cap.

The integral in Equation 3 is in principle over the entire surface, and as explained above, the formulation using anomalies is then entirely equivalent to one in global spherical harmonics. However, for our local analysis we will limit ourselves to areas on the Moon. The discretization in Equation 7 will thus only have a limited number of anomalies. This will reduce the number of estimation parameters, but it will also need to be shown that the solutions are not deteriorated by limiting ourselves to an area. The kernels in the integral equations (see Equations A12–A14 in Appendix A) determine the influence of one anomaly on the acceleration on the spacecraft: for what angle ψ_c (the angle between the location of an anomaly at the reference surface and the computation point) will the kernel value be small enough? This means that an anomaly at an angle ψ_c away from the computation point will hardly contribute to the acceleration on the spacecraft, and this can thus be used to limit the number of anomalies considered. Rather than showing the kernel functions, we show a more direct result on the actual GRAIL KBRR data in Figure 2. We computed the effect of one gravity anomaly with an amplitude of 1 mGal (1 mGal = 10^{-5} m/s^2) and a spatial size of l / 6° by l / 6° on a KBRR measurement at two different altitudes: at 55 km (the PM altitude) and at 23 km (the XM altitude). We computed this effect by processing actual GRAIL KBRR data with and without this anomaly in the force model. We then plot the difference in KBRR residuals, which thus show some noise. Figure 2 shows that the influence quickly diminishes away from the center point of the anomaly, and for the XM data is limited to about 5° from the anomaly center. Smaller anomaly sizes will have an even more limited effect. When the midpoint of the two spacecraft is directly over the center of the anomaly, the two spacecraft essentially experience the same effect, and the KBRR value is zero. The PM altitude is higher and so the effect is smaller. The maximum KBRR value of about 0.25 μm/s is roughly 5–8 times the noise level of the KBRR data (e.g., Konopliv et al., 2014; Lemoine et al., 2014). These results confirm that the effects of anomalies on the spacecraft are limited, and that we can thus estimate only the anomalies in a given area

without estimating anomalies over the entire globe. We will discuss boundary effects on the solutions in detail in Section 6.

3. Anomaly Estimation and Neighbor Constraint

We start off with the general model that relates a data vector $\mathbf{d}$ to a vector of model parameters $\mathbf{x}$ through a functional relationship $\mathbf{a}$:

$$\mathbf{d} = \mathbf{a}(\mathbf{x}) + \boldsymbol{\epsilon}, \tag{8}$$

where $\boldsymbol{\epsilon}$ is the noise vector, which will be assumed to be a zero-mean, Gaussian process with covariance $\mathbf{P}$. This is in general a nonlinear equation. We apply a Gauss-Newton method (e.g., Seber & Wild, 1989) that linearizes this equation, and then solves it through iterations. For the kth iteration, the updated gravity anomaly vector $\Delta\mathbf{g}_{k+1} = \Delta\mathbf{g}_k + \Delta\mathbf{x}_k$, where $\Delta\mathbf{x}_k$ is the kth adjustment to the anomalies from the linearized equation. This could also be expressed as an adjustment to $\Delta\mathbf{g}_k$ and would thus be $\Delta\,\Delta\mathbf{g}_k$, but for clarity we will use $\Delta\mathbf{x}_k$.

The discretization described in Section 2.2 allows for the generation of measurement partial derivatives with respect to the gravity anomalies in our data processing software, GEODYN II (Pavlis & Nicholas, 2017). We describe the data processing itself in detail in Section 4. We consider the kth iteration of the Gauss-Newton method, and subscripts k refer to this iteration. If the partial derivatives of KBRR data residuals $\mathbf{r}_{d,k}$ (a vector with dimension $N \times 1$, where N is the number of data points) with respect to gravity anomalies $\Delta\mathbf{g}_k$ (a vector of dimension $M \times 1$, with M the number of estimated parameters) are given as $\mathbf{A}_k$ (an $N \times M$ matrix), then the linearized observation equation that relates gravity anomalies to KBRR data residuals reads in standard form:

$$\mathbf{r}_{d,k} = \mathbf{A}_k\,\Delta\mathbf{x}_k + \boldsymbol{\epsilon}, \tag{9}$$

where $\Delta\mathbf{x}_k$ is the kth anomaly adjustment, and $\Delta\mathbf{g}_{k+1} = \Delta\mathbf{g}_k + \Delta\mathbf{x}_k$. The matrix $\mathbf{A}_k$ is called the sensitivity matrix and it relates the observables to the estimated parameters—Equation 9 thus establishes the link between the two. This matrix is obtained from numerical integration of the variational equations, which describe the sensitivity of the state vector with respect to the estimated parameters. The variational equations are derived from the basic equations of motion, and this can be found in standard works on orbit determination such as Montenbruck and Gill (2000) and Tapley, Schutz, and Born (2004). In addition, examples of works that relate KBRR data to the gravitational potential can be found in Han (2004, 2013).

The construction of Equation 9 is based on Equation 3 which is an integral equation of the first kind, and these are known to be ill-posed (e.g., Groetsch, 1993). This requires regularization: the use of additional, a priori information. In our earlier work, we followed Rowlands et al. (2010) and Sabaka et al. (2010) who applied neighbor smoothing in their analysis of mascon estimation using GRACE data, and here we do the same. Each anomaly in the grid Δg_i is assumed to be equal to any other anomaly Δg_j. Therefore, the constraint reads $\Delta g_i - \Delta g_j = 0$ with $i \neq j$. Each constraint pair between anomalies Δg_i and Δg_j is weighted depending on the distance between the anomalies on the sphere, d_{ij}, with a weight $W_{c,ij} = \exp(1 - d_{ij}/D)$, where D is the correlation distance. We set the latter equal to the latitudinal size of the anomaly Δg_i (Rowlands et al., 2010). Note that this is a natural choice: larger values for D may lead to over-smoothing because the constraint would still be relatively strong for anomalies further away. By choosing the latitudinal size, variations between anomalies clustered relatively close together can still be obtained. Expressions for the covariance of anomalies expressed in spherical harmonics also exist (e.g., Bills & Ferrari, 1980; Tscherning & Rapp, 1974), most often used in least squares collocation estimation techniques (e.g., Moritz, 1978). These can also be used to determine the correlation distance, but we did not pursue this because we use discrete anomalies. This results in a constraint weight matrix $\mathbf{W}_c$, and the use of weights between pairs based on their distance prevents the solution from having one uniform value where all anomalies would be the same.

Our gravity anomalies $\Delta\mathbf{g}_k$ are themselves perturbations to an underlying global gravity field model that is used in the analysis of GRAIL data. This global model stays fixed as the anomalies are updated. We use one of our recent models, GRGM1200 A (Goossens et al., 2016, 2020), which is a model in spherical harmonics of degree and order 1200.

Finally, instead of applying the smoothing to the gravity anomalies $\Delta\mathbf{g}_k$ only, we apply the smoothing to the entire gravity field. Since the anomalies, we estimate are additional anomalies to the underlying background model, this means that the smoothing will be applied to $\Delta\mathbf{g}_k + \Delta\mathbf{g}_{\text{global}}$, where $\Delta\mathbf{g}_{\text{global}}$ are the anomalies from the global model, GRGM1200 A, computed from Equation 4. This results in the following constrained solution for the adjustments $\Delta\tilde{\mathbf{x}}_k$:

$$\Delta\tilde{\mathbf{x}}_k = \left(\mathbf{A}_k^T\mathbf{W}_{d,k}\mathbf{A}_k + \mu\mathbf{D}^T\mathbf{W}_c\mathbf{D}\right)^{-1}\left(\mathbf{A}_k^T\mathbf{W}_{d,k}\mathbf{r}_{d,k} + \mu\mathbf{D}^T\mathbf{W}_c\mathbf{r}_c\right), \tag{10}$$

where $\mathbf{W}_{d,k}$ is the data weight matrix, which is diagonal with entries $(1 / \sigma_i^2)$ where σ_i is the data weight for a data point , $\mathbf{D}$ is the matrix with the constraint partial derivatives, μ is a scale factor applied to the constraint (in addition to the weight matrix $\mathbf{W}_c$), and $\mathbf{r}_c$ is the vector with constraint residuals which is expressed as $\mathbf{r}_\mathbf{c} = -\mathbf{D}\Delta\mathbf{g}_{\text{global}}$. The constraint between two anomalies Δg_i and Δg_j is written as $\Delta g_i - \Delta g_j = 0$ and thus the partial entries for Δg_i are one, those for Δg_j are negative 1, and those for all other anomalies in a row of the partial matrix are zero. We note that parameters other than gravity parameters (such as those related to the GRAIL spacecraft orbits as explained in Section 4) are not included in $\Delta\mathbf{x}_k$. Instead, they are taken into account through their Schur complement (Sabaka et al., 2010). For each kth iteration, the entries $\mathbf{A}_k$, $\mathbf{W}_{d,k}$, and $\mathbf{r}_{d,k}$ are updated, although in general, $\mathbf{W}_{d,k}$ will stay the same (see Section 4 for the data weights used). The entries $\mathbf{D}$, $\mathbf{W}_c$, and $\mathbf{r}_c$ remain the same, but we note that on the constraint matrix, we update information on $\Delta\mathbf{g}_k$ so that the data matrix $\mathbf{A}_k$ and the constraint matrix have the same start state.

On a final note, we remark that our neighbor constraints are isotropic in their weighting by using one value for D for each anomaly in $W_{c,ij}$ as defined above. This can easily be changed by varying D, to account for, for example, more smoothing in the east-west direction than in the north-south direction. The latter can be desirable because of the polar orbit of the GRAIL spacecraft that results in striping in the solutions that the neighbor constraint can overcome (Goossens et al., 2014). We tested this by computing the azimuth between two anomalies, and by defining an ellipse where the correlation distance is larger in east-west direction. Test results did not show improvements and so we did not pursue this further.

4. Determining the Optimal Short-Arc Processing

We will process the data and estimate the GRAIL orbits over continuous time spans, which are called arcs. In standard processing for the global models, these are several days long. A trade-off for arc length exists between balancing sensitivity with respect to long-wavelength features of the gravity field on one hand, and limiting the build-up of errors due to mismodeling of for example nonconservative forces on the other hand. Because we will estimate anomalies in a selected area, we will also only select data over that selected area, and our arcs have the length of the time it takes for the spacecraft to cross this area. This means that our arcs will be short. We can do this by the virtue of using a different parametrization for the GRAIL orbits, and by using results from our global analysis. The arc lengths depend on the size of the solution patches, which we list below in Table 1. In our analysis, the areas are of similar size in latitude, which results in arcs of typically 22 min long for the rectangular patches, and 18 min for the polar caps.

We base our analysis of the KBRR data on the approach in Rowlands et al. (2002). There it was shown, in the framework of the GRACE mission, that it is possible to estimate the gravity field using short arcs. Instead of the 12 Cartesian positions and velocities, they used a baseline formulation for the two spacecraft, transforming the Cartesian coordinates into a spherical representation. In Rowlands et al. (2002), it was shown that it is sufficient to adjust 3 parameters instead of 12, as these parameters are the most sensitive to the KBRR data. These three parameters are: the pitch of the baseline vector between the two satellites, the baseline velocity vector's magnitude, and the baseline velocity vector's pitch. This has been applied successfully to the analysis of GRACE data (e.g., Loomis et al., 2019; Luthcke et al., 2006, 2013; Rowlands et al., 2005), and we also applied it in our earlier local GRAIL analysis (Goossens et al., 2014). Our global analysis also estimates empirical accelerations, as detailed in Goossens et al. (2020). Here, we tested the effects of these accelerations, and of using either long arcs or short arcs.

First, we tested three different scenarios with respect to the accelerations, using short arcs: not including them, including them but not estimating them, and including and (re)estimating them. We use the values

Table 1
Summary of Parameters Used in Local Gravity Field Determination

Area #	Longitude extent	Latitude extent	Constraint weight μ	Late XM weight	Cap radius (°)	L_{win}
1	[−5.1,49.95]	[−9.9,65.1]	10^{-3}	0.1	27.525	14
2	[−5.1,49.95]	[−61.95,9.9]	10^{-4}	0.1	27.525	14
3	[44.85,110.1]	[−9.9,65.1]	10^{-3}	0.1	32.625	12
4	[44.85,110.1]	[−61.95,9.9]	10^{-3}	0.1	32.625	12
5	[105,169.95]	[−9.9,65.1]	10^{-4}	0.1	32.475	12
6	[105,169.95]	[−61.95,9.9]	10^{-4}	1.0	32.475	12
7	[164.85,219.9]	[−9.9,65.1]	10^{-5}	1.0	27.525	14
8	[164.85,219.9]	[−61.95,9.9]	10^{-5}	0.1	27.525	14
9	[214.8,289.95]	[−9.9,65.1]	10^{-4}	1.0	37.5	10
10	[214.8,289.95]	[−61.95,9.9]	10^{-5}	0.1	35.925	11
11	[284.85,360]	[−9.9,65.1]	10^{-3}	0.1	37.5	10
12	[284.85,360]	[−61.95,9.9]	10^{-3}	0.1	35.925	11
13 (north pole)	[0,360]	[60,90]	10^{-4}	0.1	30.0	13
14 (south pole)	[0,360]	[−90, −56.85]	10^{-4}	0.1	30.0	13

for the start orbit and empirical accelerations that were determined from the longer arc. We show results in Figure 3. The test area was that for Mare Orientale, following a similar analysis as presented in Zuber et al. (2016). For this test, the background global model was a degree and order 1080 model, a predecessor to our later GRGM1200 series (Goossens et al., 2016, 2020). We generated local solutions for this area, with a grid size of 0.15° by 0.15°, which is equivalent to degree and order 1200 in spherical harmonics. We then compute localized correlations between gravity and topography using one taper for a spherical cap centered on 270°E, 25°S with a radius of 25° and a windowing bandwidth of L_{win} = 16 such that the taper has a concentration factor better than 99.99%. The solution based on orbits where the accelerations are not included has slightly worse correlations than the other two solutions, as can be seen in Figure 3a. The difference between solutions that include and either estimate or not estimate the accelerations is small (not shown). We decide to include and estimate the accelerations in our analysis, especially since the use

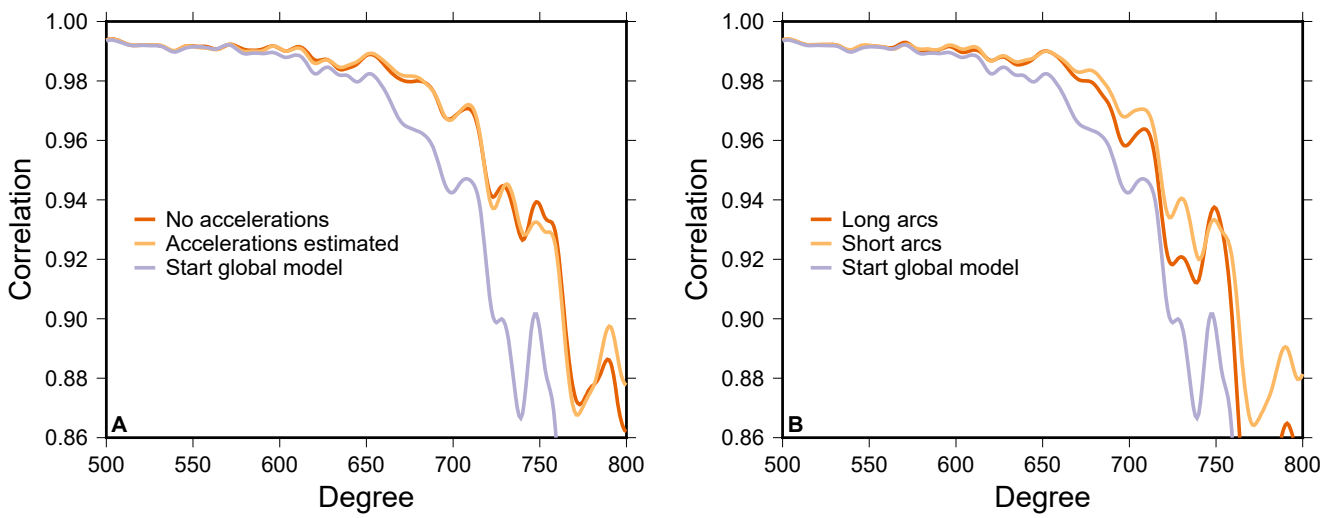

Figure 3. A comparison in terms of localized correlations with topography of various solutions for the test area of Mare Orientale based on different parametrizations of the orbit determination process (a), and on different arc lengths (b). For comparison, we also include the correlations with the global start model.

of these accelerations can act to absorb mismodeling effects, and the results show that their inclusion does not adversely affect the solution.

Our analysis so far is based on short arcs using data selected over the area of interest. One other way of processing would be to use the longer arcs from the global analysis with the same baseline formulation and data selection. We would then use KBRR data only, again start from the previously determined orbit, and readjust the three baseline parameters and selected accelerations. This is how GRACE data are processed for mascons or monthly spherical harmonic models at Goddard Space Flight Center (GSFC; e.g., Luthcke et al., 2006). The advantage of this processing would be fewer arc parameters: each short-arc has three baseline parameters. The number of empirical accelerations would not change: we estimate multiple sets of empirical accelerations per orbit (Goossens et al., 2020) and each passage over an area is separated by one orbit by definition. However, the results in Figure 3b show that the long-arc solution has lower correlations than the short-arc solution. Again, the differences are not big, and the figure also indicates that the long-arc solution performs much better than the global start model. Nonetheless, we decided to process the GRAIL data using short arcs, where we include and estimate the empirical accelerations.

5. Determining the Optimal Local Solution Per Area

For each area, we will determine the gravity solution using Equation 10. We process the GRAIL data using short arcs as explained above with only data over the selected area. This results in a partial derivative matrix $\mathbf{A}$ and residuals $\mathbf{r}_d$ for each short arc. The entries for the data weight matrix $\mathbf{W}_d$ are straightforward: this is a diagonal matrix with elements $1 / \sigma_i^2$ on the diagonal, where σ_i is the data weight applied in orbit determination. We used a weight of 0.03 μm/s for PM data and 0.05 μm/s for XM data, following the reported noise levels (Konopliv et al., 2014; Lemoine et al., 2014). We can then form the normal matrix system, and the neighbor smoothing constraint matrix (and its accompanying right hand side). We form separate matrices for the PM data, for early XM data (before December 2012) and for late XM data (after December). We make the distinction so that we have the option to apply different weights to each system when combining the normal systems. Late December data are taken at a lower altitude, and while they contain more information about the small-scale gravity field, our earlier analysis found that down-weighting the December data improved the solutions (Goossens et al., 2014).

We will determine the optimal local solution for each area by varying the remaining input parameters: the weights on the data matrices, and the constraint scale factor μ. For each solution, we will then transform the anomalies into spherical harmonics, and compute localized correlations with topography. We will select the combination of weights that results in the best overall correlations. We will keep the PM and early XM data weights at 1 and will choose the late XM data weights to be 0.1, 0.5, or 1. For μ, following our earlier analysis results (Goossens et al., 2014), we will choose values of 10^{-3}, 10^{-4}, and 10^{-5}. We did not find that fine-tuning these values further made any appreciable difference in the solutions. We also found that using a technique such as variance component estimation (e.g., Kusche, 2003) does not result in solutions with improved correlations over the solutions already obtained. Eventually, this means that we compute nine separate solutions for each area, and then evaluate each solution in terms of localized correlations with topography.

We demonstrate this with the results shown in Figure 4. For one of our areas (see Section 7.1 for further details), focused on the nearside with bounds −5.1°E to 49.95°E, and 9.9°S to 65.1 N, we determined nine solutions, and computed localized correlations. The localized correlations are again computed with one taper, centered on the center point of the area under consideration. The cap radius is computed such that the cap fits entirely inside the area. For the example under consideration here, the center points are 22.4256°E, 27.6°N, and the cap radius is 27.525°. The concentration factor of the taper is again chosen to be larger than 99.99%, resulting in $L_{\text{win}} = 14$. In Figure 4a, we show solutions with varying constraint weights μ (while the late XM weight was kept at 0.1). For this area $\mu = 10^{-3}$ gives the best overall correlations, but the difference with the solution using $\mu = 10^{-4}$ is small. Figure 4b shows the results when we vary the late XM weight, this time using $\mu = 10^{-3}$ for all the solutions. The differences between the solutions are minimal, with a weight of 0.1 for the late XM data having marginally better correlations. For this solution, we thus select the combination $\mu = 10^{-3}$ with a late XM weight of 0.1. In Section 7.1, we will introduce our chosen areas and show the results for the resulting constraint and data weight factors.

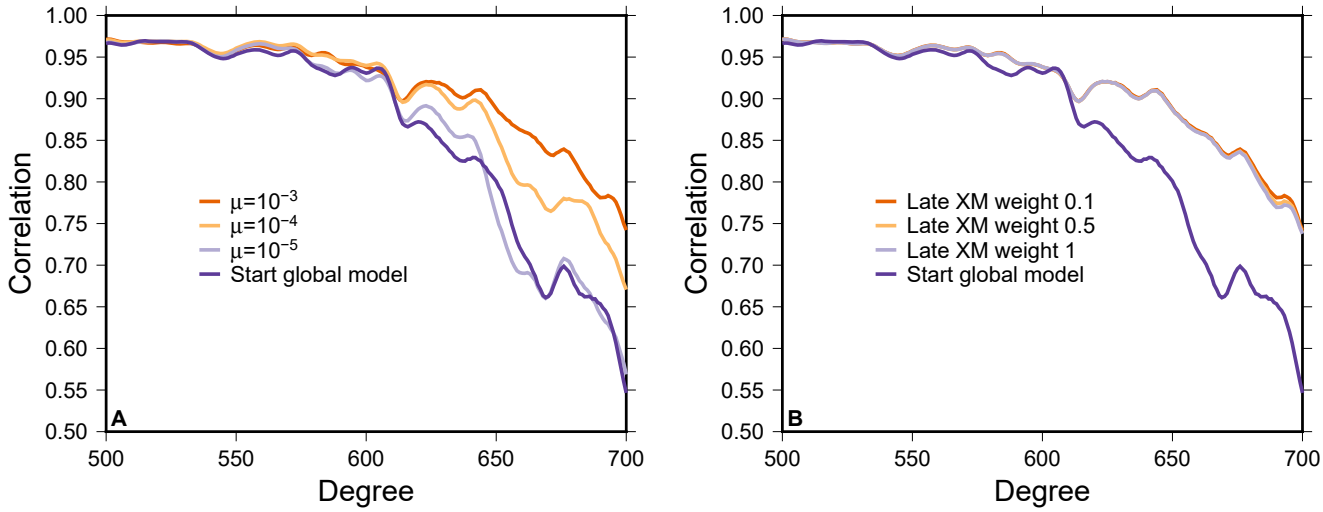

Figure 4. A comparison in terms of localized correlations with topography of various solutions for a test area focused on the nearside (−5.1°E to 49.95°E, and 9.9°S to 65.1°N) based on different constraint weights (a), and on different weights for the late XM data (b). For comparison we also include the correlations with the global start model.

6. Combining the Local Solutions

After we determine the set of local solutions, we need to consider how to combine them into one map. As discussed in Section 2.2, and shown in Figure 2, the effects of one anomaly are limited to about 5° away from that anomaly, depending on the anomaly size and data altitude. We limit our analysis to selected areas on the Moon using data from when the spacecraft are over that area. Invariably, this means that anomalies at the boundaries of the area will be affected because data points close to them would also have effects from anomalies just outside of the area. In addition, longer wavelengths (larger than the area size) can also not be recovered well. Such boundary effects are well known in local studies. The standard remedy for this is to discard the solution at the edges because the cells there are most affected. We apply the same method here. From Figure 2, we determine that an overlap of at least 5° between solutions should exist. Longer wavelengths will be less of an issue since our analysis uses a background global spherical harmonics model and we estimate only adjustments to this model.

Next, we consider how to patch the overlapping solutions together. One of the most natural ways to patch the solutions is to split the overlap from two regions symmetrically, and take for each part of the overlap the solution whose boundary is not contained in that part. That way, boundary effects would vanish. For the sake of completeness, we also consider patching solutions where the overlap is taken fully from either the original (central) solution or the added patched solution. In addition, a solution where both sets of anomalies from the overlapping solutions are blended to obtain a solution in the overlap is also computed. Such a blend gives zero weight outside the regions, a weight of one in the interior of each region (but not in the overlap) and a 2-D cosine tapered weight in the overlap. We illustrate these different patching methods in Figure 5, where we have two solutions with different, constant anomaly values (10 and −10 mGal, to clearly note the difference between the two) that we patch according to the different methods. The overlapping area is in the middle of the maps in Figure 5, and indicated with white lines. The dash-dot line indicates the central overlapping meridian. For the symmetrical overlap in Figure 5c, it is clear that half of the overlap comes from the central (10 mGal) solution, and the other half from the −10 mGal solution, such that their respective boundary parts are not included. For the solutions where we either keep the central part (Figure 5a) or the added part (Figure 5b) it is clear we only have those values in the overlapping part. The blend method (Figure 5d) clearly mixes the two smoothly. To evaluate the patching, we again compute localized correlations, this time centered on the overlapping region. We focus on patching the east-west borders and the north-south borders.

Before investigating the various patch methods, we stress the importance of selecting the grids carefully. If the grid is not selected such that overlapping regions have the same nodes, interpolation is required to patch

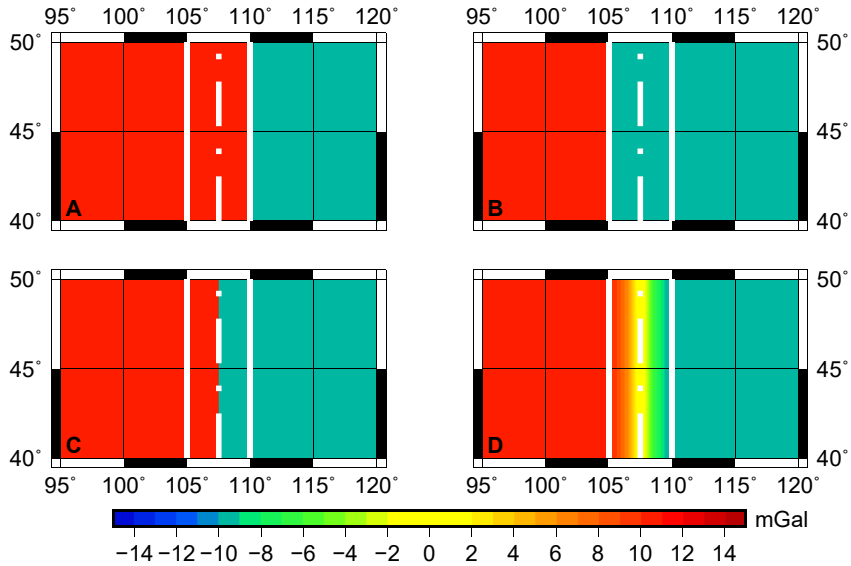

Figure 5. Examples of different patching methods. We patch one anomaly field (in this case with a constant value of 10 mGal) with another field (with a value of −10 mGal) on the eastern border of the former. The overlapping area is indicated with lines, and the central meridian of the overlapping are is indicated with a dash-dot line. We can keep the entire central solution (a), or the added eastern solution (b), or we can do a symmetrical overlap where the boundaries of each solution are excluded (c), or we can blend the solutions with a taper (d).

them, which modifies the solution. The effects of this interpolation were tested, and we show the results in Figure 6. When no interpolation is required, we obtained the best correlations. While the correlations for the grids where interpolation was required are still better than those for the global start model, the difference here are considerable, unlike in earlier cases in Figures 3 and 4. We will thus match our grids such that the overlapping parts share the same nodes (which comes down to selecting one global regular grid that is divided into overlapping regions), as we show in Section 7.1.

In Figure 7, we show localized correlations with topography for solutions with the different patching methods. The central area under consideration in this example extends from 44.85°E to 110.1°E, and 9.9°S to 65.1 °N. We evaluate correlations on the south (Figure 7a) and east (Figure 7b) borders for this solution. These neighboring areas (see also Section 7.1) extend from 61.95°S to 9.9°N for the area to the south (the longitude extent is the same as for the area under consideration) and from 105°E to 169.95°E for the area to the east

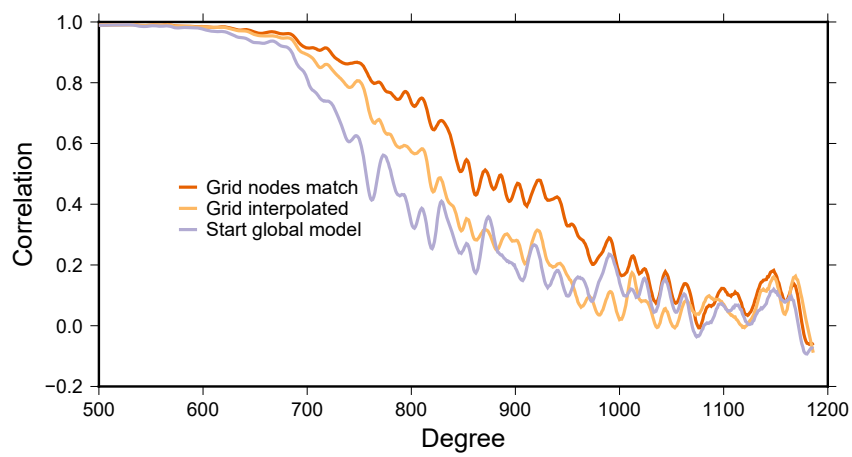

Figure 6. Localized correlations with topography for a solution where the grid nodes in two neighboring grids match for patching, and for a solution where interpolation is required. For comparison, we also include the correlations with the global start model.

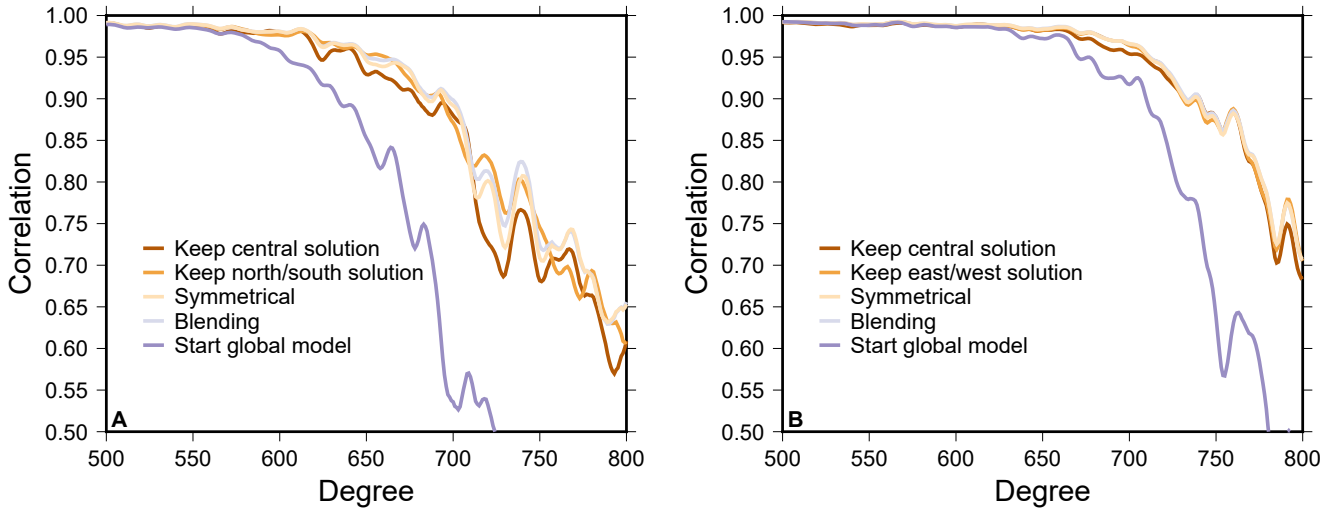

Figure 7. Localized correlations with topography for solutions with different patching strategies for the south border (a) and for the east border (b). For comparison we also include the correlations with the global start model.

(here, the latitude extent is the same). This means that the overlap in the east direction is 5.1° and that in the southern direction is 19.8°. For the correlations on the southern part, the spherical cap is centered at 77.475°E, 0°N, with a radius of 32.625°. Using one taper with a concentration factor of 99.99% this results in $L_{\text{win}} = 12$. For the eastern part, the cap is centered at 107.55°E, 27.6°E, with a radius of 37.5° and $L_{\text{win}} = 10$. Solutions where we keep either the central part or the additional (south, or east) part in the overlapping region do not take the boundary effect into account, and as expected they have slightly worse correlations than the symmetrical or blend patch method. The difference between the latter two is very small. The smaller overlapping region at the eastern border also does not appear to pose an issue for the patched solution as the correlations in Figure 7b do not show any deterioration. We also note that north-south boundary effects could potentially be larger, because of the polar orbits of the GRAIL satellites: the short arcs will start or stop at a north-south border to state-vector effects could also be present at those borders. However, our patched solution here and its evaluation using correlations show no signs of adverse effects, indicating that our selection of the size of the overlap is appropriate. We will also show in Section 7.2 that the entire patched solution does not have any remaining boundary effects. In conclusion, because the differences between the symmetrical and blending method are small, we choose the symmetrical patching method for all regions. Our software script that patches the solutions would allow for a different patching type for each area and border.

7. Results and Discussion

In this section, we will show and discuss the resulting global map of lunar gravity, consisting of a set of patched local solutions. We will first introduce the chosen grid and areas, together with the solution parameters. We will then show and discuss the results.

7.1. Local Areas: Bounds and Solution Parameters

As explained in Section 6, care has to be taken to define the grids of different solutions to avoid interpolation when patching them. Here, we list the chosen grids, with overlaps, which are the result of a global, regular $0.15° \times 0.15°$ grid. When transforming this into spherical harmonics, this is equivalent to a model of degree and order 1199 (we use 1199 instead of 1200 because our grid spacing uses $L_{\text{max}} + 1$ for its spacing: $180/(L_{\text{max}} + 1)$). Our start global model is the degree and order 1200 model GRGM1200A (Goossens et al., 2016, 2020). This will also allow us to compare our new global map with the standard start model and its global iterated version, GRGM1200 B.

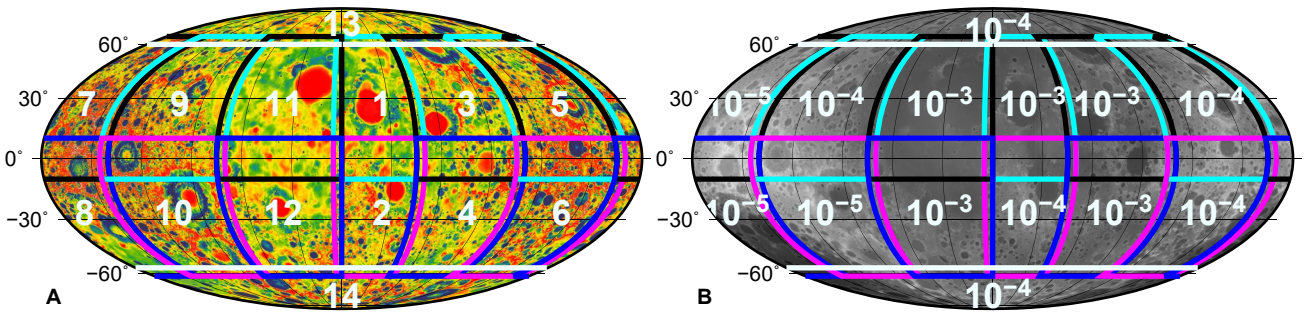

Figure 8. We indicate the areas on a map of gravity anomalies from the global start model GRGM1200 (a), and the constraint weight factors for each area, shown on lunar topography from LOLA (b). The map projection is a Mollweide projection centered on the nearside.

In Table 1, we show the boundaries of our chosen areas, and the selected constraint and data weight parameters from our solution analysis. These parameter values are the final values used in our solution, which we iterated. We explain this in more detail below. The table also includes the values for the cap radius and windowing bandwidth value L_{win} that were used in the localized correlation computations to determine the optimal constraint weight and data weight. In order to get a better sense of the overlaps for the areas, we show the areas on a map of gravity anomalies from the global start model in the background in Figure 8a. We also show the constraint weights, with topography in the background, in Figure 8b.

7.2. Combined Solution

We present our combined solution in Figure 9, where we show the global map of lunar gravity that is the result of our determination of 14 separate local solutions. We applied regionally varying constraint weights as given in Table 1 and as shown in Figure 8b. We patched the solutions together using the symmetrical method for all boundaries on all regions. The map in Figure 9 is at the full resolution of the model, $0.15° \times 0.15°$. We plot the discrete gravity anomalies at this resolution, but it also means that the maximum degree L_{max} that would be used in Equation 4 is 1,199, the spherical harmonics resolution of our local models as explained above. We discuss this resolution further below. We also include Bouguer disturbances, computed by subtracting the contribution of gravity from topography using a constant crustal density of 2,500 kg m^{-3}. We use the formulation of Wieczorek and Phillips (1998) that accounts for finite amplitude relief, and we raise topography to the 20th power, which for the Moon results in negligible errors for the Bouguer correction (Wieczorek, 2015). We compute the Bouguer disturbances between degrees 7 and 700, in order to exclude signals from the deep interior, and noise in the higher degrees. These Bouguer disturbances can be used to infer density variations in the crust (e.g., Besserer et al., 2014; Goossens et al., 2020; Han et al., 2014).

We iterated our local solutions twice (i.e., $k = 2$, following the Gauss-Newton method as introduced in Section 3), to obtain the map presented in Figure 9. For clarity, that means that in Figure 9, we show $\Delta\mathbf{g}_{\text{global}} + \Delta\mathbf{g}_2 = \Delta\mathbf{g}_{\text{global}} + \Delta\mathbf{x}_2 + \Delta\mathbf{x}_1$, in the formulation of Equation 10. Iterating the solutions assures that one can test whether the solution has converged. This is often assumed in inverse problems, but not always shown. Even if the initial adjustments are relatively small, iterated solutions can still show improvements. For example, Luthcke et al. (2013) showed that their iterated mascon solutions improved significantly, particularly in the ability to restore more signal strength. For our iterated solution, after determining an initial set of gravity anomalies ($k = 1$), we reprocessed the GRAIL data by using this initial set of anomalies in the spacecraft force model (in addition, of course, to the fixed background global model). We again determined nine solutions for each area, using different constraint scale factors and data weights. As stated in Section 3, we updated the constraint matrix with a start value for the anomalies that is now different from zero, i.e., for $k = 1$, $\Delta\mathbf{g}_0 = \mathbf{0}$, and for $k = 2$, we have $\Delta\mathbf{g}_1$ from Equation 10. We evaluated these new nine solutions again by investigating localized correlations. While we mostly expected to use the same constraint weights and data weights as in the initial adjustment, we found that we could relax the constraints over the poles, from a factor of 10^{-3} to 10^{-4}. All other factors stayed the same. The initial factors for the poles could probably have been chosen at 10^{-4} already when the initial solution was determined.

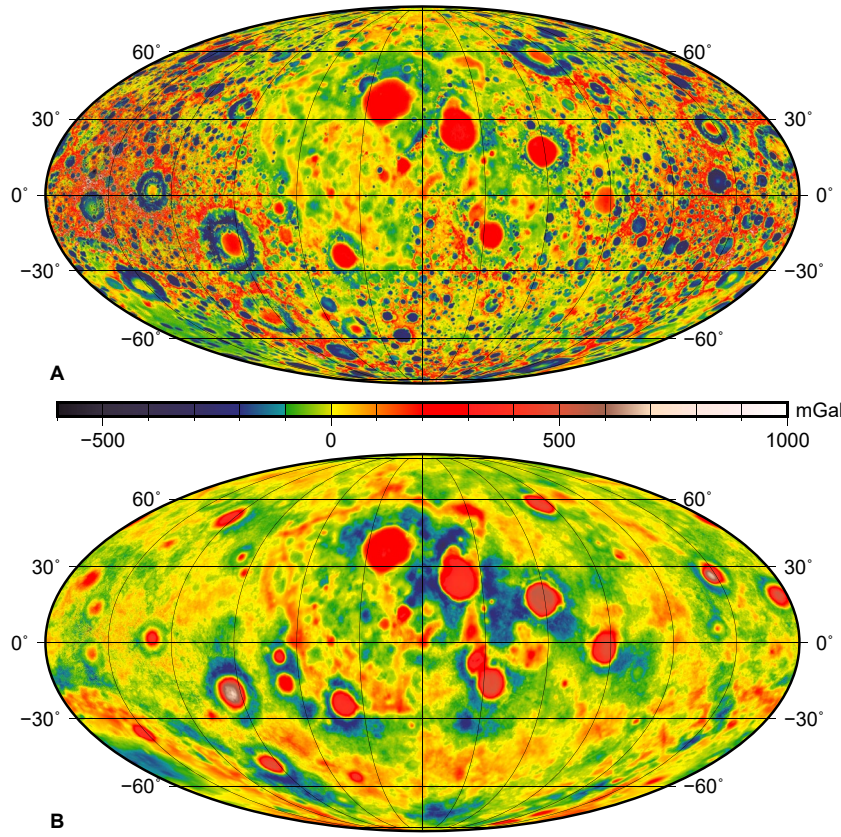

Figure 9. The global map of lunar gravity anomalies generated from our local solutions, at its full resolution of 0.15° × 0.15° (top, a), and Bouguer disturbances for the local solution, for the degree range = 7–700, using a constant crustal density of 2,500 kg m^{-3} (bottom, b). The map projection is a Mollweide projection centered on the nearside.

In Figure 10, we show the adjustments to the global model for both iterations. This map shows best that there are no boundary effects or seams visible in the solution. We also highlight that both maps use a different color scale, because the adjustments for the iterated solution are smaller than those for the initial solution: the RMS of the initial adjustment is 30.85 mGal, with values ranging from −1,003 mGal to 741 mGal. The RMS of the iterated adjustment is much smaller, at 5.75 mGal with values ranging from −237 to 239 mGal. For comparison, the anomalies at full resolution from GRGM1200 A have an RMS of 137 mGal with values ranging from −1,746 to 2,622 mGal. This shows that indeed the iterated solution produces only small, additional adjustments. We illustrate this point further in Figure 11, where we show histograms of anomaly adjustments for both solutions. This figure clearly shows the difference between the solutions, with the iterated solution showing a much narrower peak centered around 0 mGal. Because we did not find large improvements locally for the solutions, we did not do an additional iteration. In Figure 10, the largest additional adjustments in the iterated solution can be seen over the poles because we used a looser constraint there. Additional individual tracks can also be seen to have been adjusted in the iterated solution, but overall, as the histogram from Figure 11 also indicates, the additional adjustments are small.

7.3. Discussion

We now evaluate the local solutions by again computing correlations with topography. In Figure 12, we show both global correlations, and correlations localized over the south pole (with a cap radius of 30° and $L_{\text{win}} = 13$), as well as the power spectrum and effective density spectrum. The power spectrum $\sigma(l)$ is defined as:

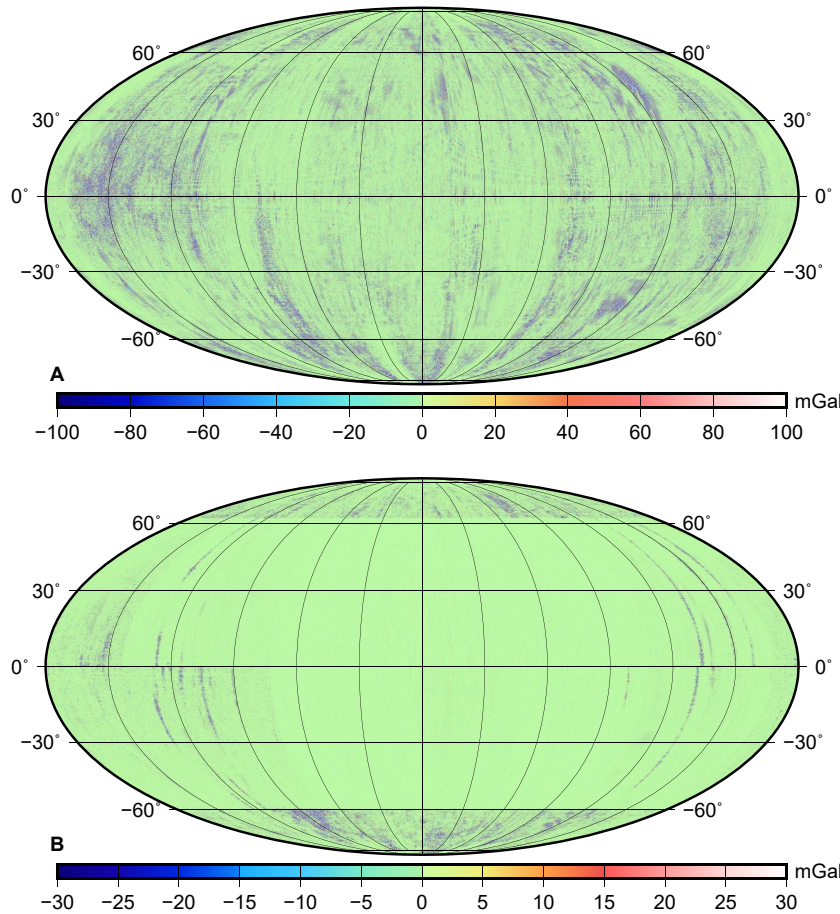

Figure 10. Adjustments for all the 14 local solutions, for the initial local model (top, a), and the iterated local model (bottom, b). In the formulation of Equation 10, this means we show the adjustments $\Delta\mathbf{x}_k$ ($k = 1$, top, and $k = 2$, bottom), and not the anomalies $\Delta\mathbf{g}_k$. As such, the iterated adjustments are additional to the first adjustments. We note that both figures have a different color scale. The RMS of the first adjustments is 30.85 mGal, and the additional adjustments have an RMS of 5.75 mGal. The map projections are Mollweide projections centered on the nearside.

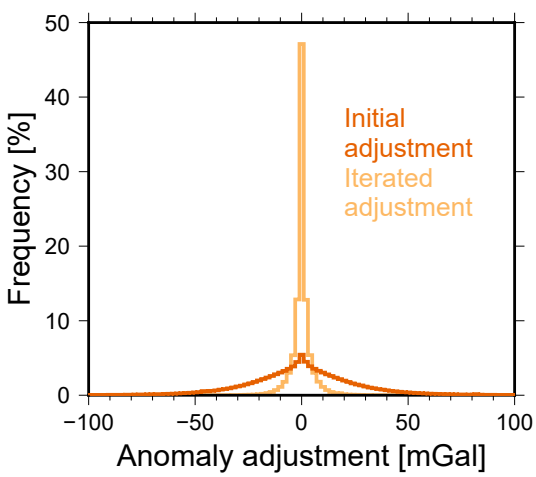

Figure 11. Histograms of the anomaly adjustments for the initial ($k = 1$) and iterated ($k = 2$) solutions.

$$\sigma(l) = \sqrt{\frac{\sum_{m=0}^{l}\left(\overline{C}_{lm}^2 + \overline{S}_{lm}^2\right)}{2l+1}}. \tag{11}$$

The effective density spectrum $\rho_{\text{eff}}(l)$ is a measure of crustal density at all scales, and it is computed following Wieczorek et al. (2013) and Besserer et al. (2014) as:

$$\rho_{\text{eff}}(l) = S_{g_{\text{obs}}\, g_{\text{topo}}}(l)/S_{g_{\text{topo}}\, g_{\text{topo}}}(l), \tag{12}$$

where S is the cross power as defined in Equation 5, g_{obs} is the estimated gravity (i.e., our local solution expressed in spherical harmonics), and g_{topo} is gravity from topography computed using the formulation of Wieczorek and Phillips (1998), with a constant density for the crust. We include two global models in Figure 12: the start model GRGM1200 A, and its iterated variant, GRGM1200B (Goossens et al., 2020). This allows us to compare our local model with both, and Figure 12a clearly shows that the local model has improved correlations over both the global start and global iterated model. This indicates that our local approach has an

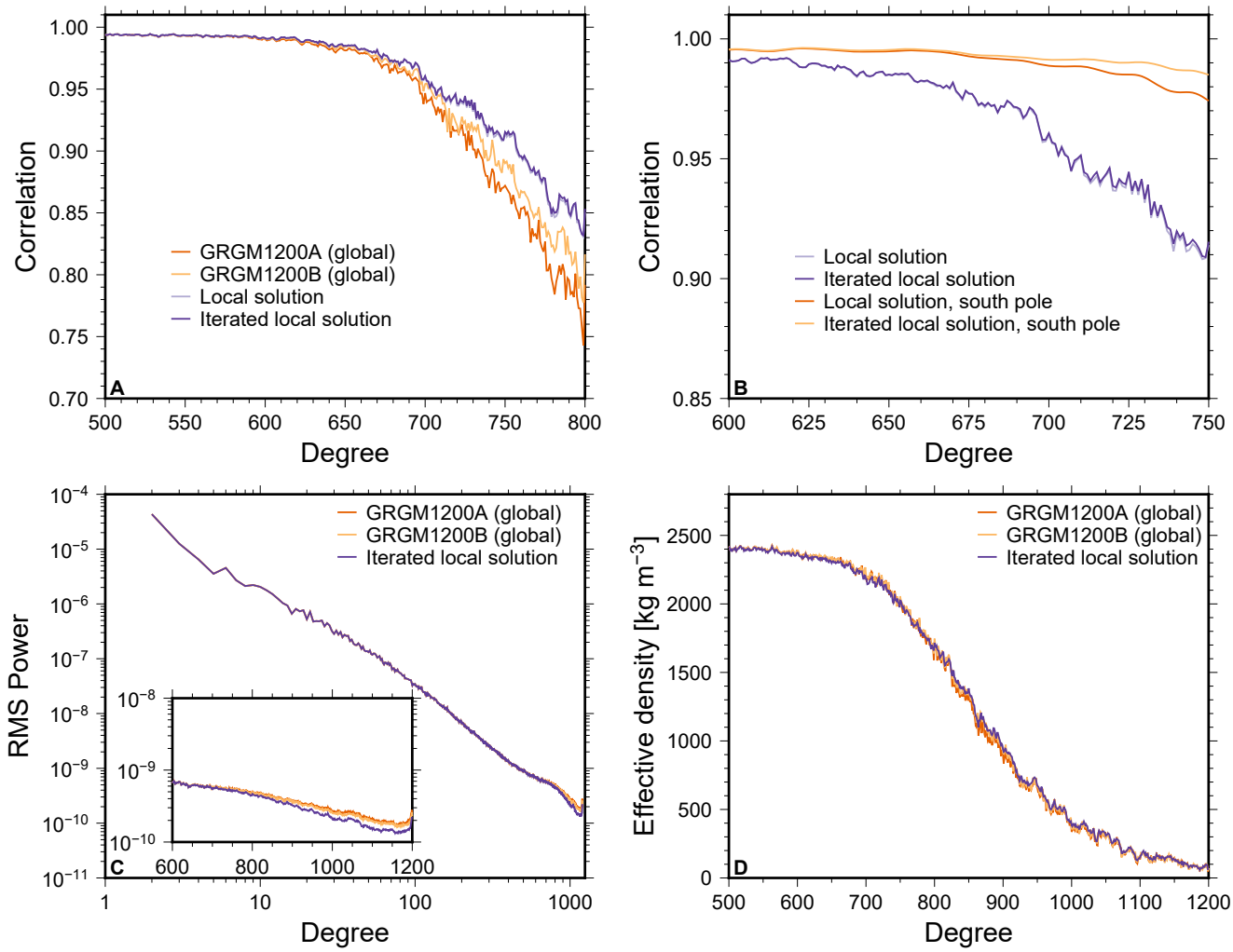

Figure 12. Global correlations between gravity and topography (a), a close up that also includes correlations localized over the south pole (b), the power spectrum of several solutions, including an inset with a close up of the higher degrees (using a linear horizontal scale, c), and the effective density spectrum (d).

advantage over processing the data into a global model. This is by virtue of being able to easily choose regionally varying constraints, as shown in Figure 8. For the global model, while not impossible (see, e.g., the regionally varying constraint that was applied by Konopliv et al. (1999) for gravity models of Venus), this is not as straightforward to implement. This was also one of the drivers behind the development of mascon solutions using GRACE data at GSFC (e.g., Rowlands et al., 2005).

The power spectrum in Figure 12c shows that up to degree $l \sim 700$, the spectra for the three models shown are very close. After this, the local model has less power, but it still shows improved correlations compared to the global models (see the inset of Figure 12c for a close up of the higher degrees). While the decrease in power could indicate that less smoothing might have been applied, we note that for each area, we selected the solution parameters with the best localized correlations, and increasing the power could thus adversely affect these. However, the effective density spectra in Figure 12d are all close. This spectrum expresses the per-degree ratio of estimated gravity and gravity from topography, and does not deteriorate with the lower power of the local model.

From Figure 8, it can be seen that the areas with less smoothing are over the farside highlands, where the topography signal is strong. Additionally, the spacecraft altitude was low because of the higher topography (Figure 1). Relatively more smoothing ($\mu = 10^{-3}$) is required over the nearside. Correlations with topography are generally lower there due to the presence of mare deposits, which make interpretation of the gravity

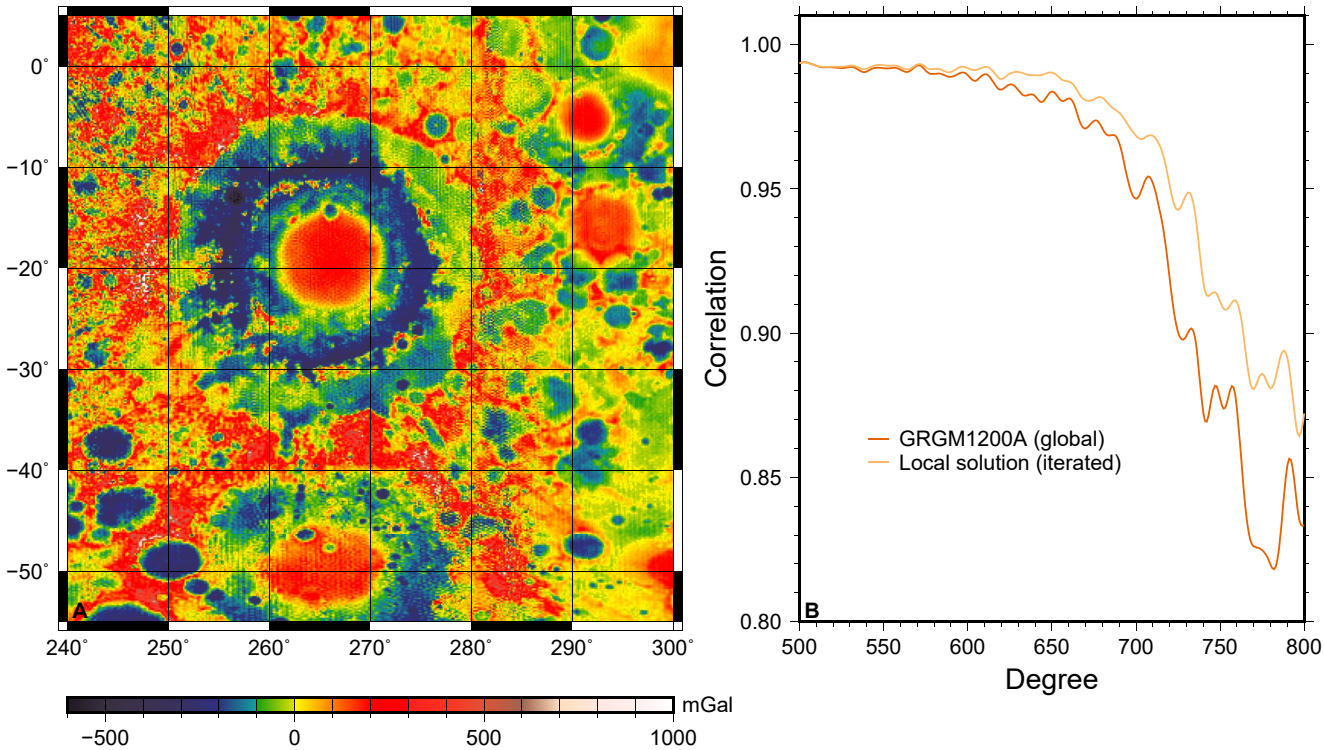

Figure 13. The local solution in terms of gravity anomalies for the Mare Orientale area (left, a), and localized correlations for various models (right, b). The map projection is an equidistant cylindrical projection centered on 260°(e) Localized correlations were centered on 270°E, 25°S, using one taper with a cap radius of 30° and $L_{\text{win}} = 13$.

field in terms of the density structure more difficult (e.g., Besserer et al., 2014; Goossens et al., 2020; Wieczorek et al., 2013). This may also indicate that despite a much better data coverage than pre-GRAIL data, a nearside/farside difference in constraints, as advocated in Han et al. (2009), could be useful.

However, inversions at this global resolution are not trivial. Our global solutions required the extensive use of the supercomputers of the NASA Center for Climate Simulation (NCCS; Goossens et al., 2020). While we also used the same supercomputers for this analysis, we needed fewer resources per solution than the global solution, as well as less CPU time. The full matrix for a global degree and order 1200 model requires 7.6 TB, and since we apply direct inversion methods, this is also the minimum memory requirement. In our local approach, the polar grids have the most parameters, and each requires about 1 TB. The other areas, being smaller, typically required several hundreds of GB. This makes the local solutions faster to compute and evaluate, which can help with determining whether the data support higher resolution models, for example, before investing the resources into determining a global model.

The correlations as shown in Figure 12a are all close together and do not appear to show substantial improvements, which can be quantified for example as the maximum degree to which the model can be used globally. The latter can be determined from when the correlations are below a certain threshold value, where the correlations can be used to derive a signal-to-noise ratio under the assumption that correlations smaller than unity are due to unmodeled signals uncorrelated with topography (Wieczorek, 2008). In Figure 12a, the difference between the initial and iterated solution is not clear, because for most of the local solutions, the correlations were very close. As explained, the biggest differences occur for the polar solutions because we used less smoothing there for the iterated solution. In Figure 12b, we show localized correlations for the south pole (with a cap radius of 30° and $L_{\text{win}} = 13$), and it is clear that the iterated solution has appreciable improved correlations with topography over the south pole (and north pole as well, which are not shown).

We further illustrate our local solution in Figure 13, where we show the local gravity anomalies for the Mare Orientale area, including localized correlations. The correlations here are markedly better than those of the

global start model, showing the improvements that the local method is capable of. If we use correlations to indicate a signal-to-noise ratio as mentioned above, then at a correlation value of 0.9 the signal-to-noise ratio is 4.3. For the global start model this occurs at (localized) degree 725 whereas this happens at degree 764 for the local model. This increase in resolution may help local studies of the upper structure of the lunar crust, which depend mostly on the high-degree terms of the models (Besserer et al., 2014; Goossens et al., 2020).

The Mare Orientale area was also the subject of study of Zuber et al. (2016), where our analysis was applied using a mixed-resolution grid. We did not pursue this in this analysis, but we note that in a way this is similar to the varying smoothing that we applied. Less smoothing can easily be seen as increasing the resolution of the model which then may require relatively more smoothing to maintain high correlations with topography.

The increase in resolution of the local models may also help in other modeling of crustal structures (e.g., Deutsch et al., 2019). The maps presented in this work are generated at the full $0.15° \times 0.15°$ resolution. If the same were to be done for the global models, they would show much more noise. The local models may thus help in delineating gravity features at the surface to a better extent, which may help their modeling.

However, we note that we cannot readily expand the spherical harmonics to its full resolution for our local model. While using the maximum degree when computing and plotting the maps of the anomalies results in much smoother maps than would be the case for an equivalent (in resolution) global model, the global and localized correlations presented here indicate that also for the local model, correlations decrease as the degrees increase. This especially would be an issue when computing the Bouguer disturbances, as shown in Figure 9b. For this, care has to be taken when determining the maximum degree to be used. If the maximum degree is used but the power in the gravity anomaly is much smaller than that for topography, the Bouguer disturbance will likely be biased by the contribution from topography (negatively, since the Bouguer disturbance equals gravity disturbance minus the topography contribution). So, while the gravity anomaly maps can be used at high resolution to map out features on the Moon, care has to be taken when converting this to Bouguer disturbances.

Several high-resolution gravity models based on GRAIL data now exist. Each has its own characteristics and advantages for use in geophysical analysis. Our local gravity model presented here has the advantage of showing smooth gravity anomalies at its full resolution, which make it suitable to study small-scale structures by better delineating gravity features, as explained above. Recently, another high-resolution gravity model was presented in Goossens et al. (2020), by applying a constraint that uses information from topography. While enforcing high correlations between gravity and topography, it was shown that this model can be used to derive lateral density variations in the lunar crust using spectral methods. We thus foresee that the local model presented in this paper is useful in analysis of structures where clear delineations of features are desired, whereas the model from Goossens et al. (2020) is useful in (localized) spectral analysis.

We did not include a full error analysis of the anomaly solutions. The covariance can readily be obtained using Equation 10, and we did investigate this for several test solutions. We found that the formal errors were generally small, with striped patterns along the tracks. However, the underlying global model has its own error and should also be included when investigating the total error for the area. In our case however, we do not take into account the full covariance of the underlying global model, as this is computationally prohibitive due to the size of the global models. With respect to the global model errors, the formal errors for the adjustments were found to be small and the total error would still be dominated by the errors for the background model. We did not further pursue this error analysis. Instead, we suggest to use covariance results from the global model GRGM1200 A, which are available at https://pds-geosciences.wustl.edu. These clone models describe deviations from the base model, GRGM1200A, computed from its covariance. These clones can be added in this case to the coefficients of the base local model instead of to GRGM1200A to create clone models for the local model. However, care should be taken when using these clone models, as they do not contain covariance information from the local models. The resulting constructed clone models will have a behavior similar to those of the GRGM1200A clones, which is counter-intuitive because correlations with topography are improved for the local model and this would suggest smaller errors for the new map of gravity.

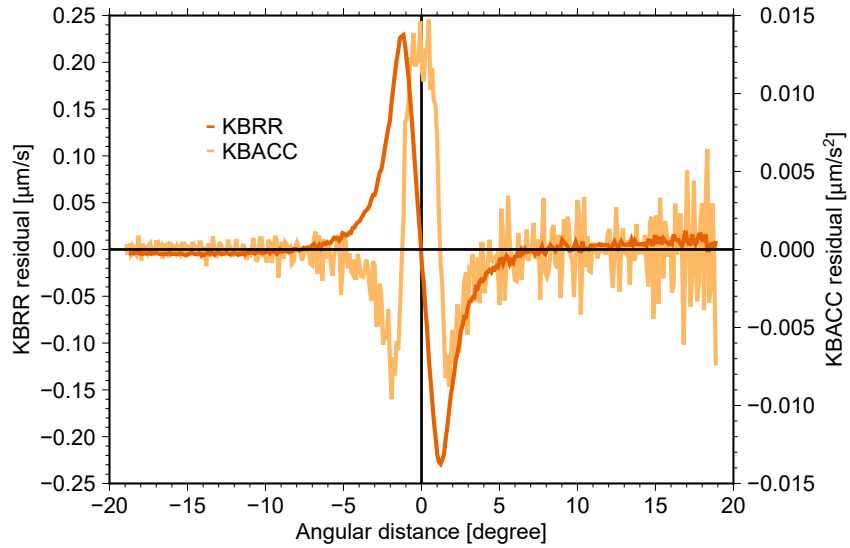

Figure 14. Similar as in Figure 2, we show the effect of a 1/6° by 1/6° anomaly with an amplitude of 1 mGal on GRAIL KBRR data, and now also include range-accelerations, for the XM altitude.

Finally, we mention an additional analysis that we performed. GRAIL data, like GRACE data, originally are range measurements that have been processed into range-rate measurements. One additional processing step would make them range-accelerations, and these are even more directly related to gravity signals, per the equations of motion that describe the acceleration due to forces. We implemented a straightforward fit using splines on the time series of residuals which were then differentiated numerically to obtain accelerations. While originally applied to Doppler data of another mission (Goossens et al., 2015, 2019), we also applied this to GRAIL KBRR data, resulting in what we call range-acceleration data (KBACC). In Figure 14, we show the effect of a 1 mGal 1/6° × 1/6° anomaly on KBRR data, the same as in Figure 2, and now we also include the range-accelerations. From this figure, it can be seen that the KBACC signal is even narrower than that of the KBRR data, which means that the KBACC data type is even more suited to localize the gravity signal, and that boundary effects might be smaller. Our fit and differentiation however does not apply additional filters, which makes the KBACC data noisier, as is easily seen. We note again that we performed this analysis using actual GRAIL data, as explained when introducing Figure 2, which leaves noise in the residuals. A similar approach, with more filtering on the data, has been reported for GRACE data as well (e.g., Tregoning et al., 2017). While analyzing GRAIL data, we also investigated solutions based on KBACC data, and found that in certain instances, these solutions outperformed the standard local solutions based on KBRR data. This was especially the case for a solution where the farside was estimated from KBACC data. We also found we could use smaller smoothing factors, although this is of course related to the amplitude of KBACC data which is smaller as Figure 14 indicates, and is thus only relative. However, when putting together our initial local solution, we repeated this analysis but found no discernible improvements (nor deterioration) compared to the standard solution. A future analysis using these data would likely benefit from investigating the filtering of the accelerations.

8. Conclusions and Outlook

We have analyzed GRAIL intersatellite KBRR data to determine local gravity field models on the Moon. We have applied a short-arc analysis where we transform the coordinates of the two spacecraft into coordinates describing the baseline between the two. We only adjust 3 from the 12 components in this representation as they are most sensitive to KBRR data: the pitch of the baseline vector between the two satellites, the baseline velocity vector's magnitude, and the baseline velocity vector's pitch. We also include and estimate any empirical accelerations acting on the spacecraft that were included in longer arc analysis for global gravity field determination, as we found that this produces the best results, where solutions were evaluated using localized correlations between gravity and topography. We divided the Moon into 12 regions and 2 caps for

the poles, and determined local solutions for each. Our solution strategy uses a global start model (a spherical harmonics expansion of degree and order 1200), and we estimate adjustments to this model, which are expressed as gridded gravity anomalies. We apply neighbor smoothing on the combination of adjustment and anomalies from the global model. For each region, we determine the optimal smoothing parameter, and an additional weight factor on December data, again by comparing localized correlations. Our regions were chosen such that they share nodes and are overlapping, in order to minimize boundary effects. We patched our solutions together using a symmetrical patching method where for each part of the overlap the solution whose boundary is not contained in that part is taken. In this way, solution boundaries are not included. Analysis found that a boundary of about 5° is sufficient.

Our patched solution shows no boundary effects. Global correlations with topography are improved when compared to the global start model, and when compared to a full iteration of our global start model. Our local solution was also iterated and we found that the iterated adjustments were much smaller and have less spread than the initial adjustments. We applied different smoothing factors for each region, and found that areas with more topography, such as the farside highlands, require less smoothing and still have high correlations with topography. While also partly related to satellite altitude above the surface, this also indicates dominance of the farside on the entire gravity signal, which is also clear from global models, when comparing nearside and farside power and correlation spectra (e.g., Lemoine et al., 2013).

Local correlations over areas such as the south pole or Mare Orientale indicate clearly that the local solution presents a substantial increase in resolution. For example, our Mare Orientale solution crosses correlations with topography of 0.9 at a (localized) degree of 764 whereas the start model does this at the lower value of 725. The maps we generated and showed are also at their full resolution of $0.15° \times 0.15°$. They show a mostly smooth and clear gravity signal, delineating feature boundaries clearly and with less noise than a global model at the same resolution would. The local model can be used in detailed analyses of the lunar crust. We do stress however that spectral analysis of the local solution should still be undertaken with care, as correlations with topography show decreasing values with increasing degree.

One other advantage of our local approach is that it requires fewer resources. While our number of parameters for each solution is still substantial, and while we still needed to resort to the use of supercomputers to estimate the solutions, they do require less memory and computational nodes (and as a consequence, less CPU time) than a standard global model estimation does.

We briefly discussed the use of range-accelerations instead of the standard Ka-band range-rate data. While initial results were promising, we found that there was no further improvement for our final analysis. However, additional research into filtering these accelerations may improve the solutions, because accelerations are more directly related to gravity and should thus be able to describe small-scale features well, as our test results showed. In addition, we also briefly explored the use of different correlation distances in the neighbor constraints, to obtain more smoothing in the east-west direction compared to the north-south. The latter can be desirable because of striping in the solutions as a result of the polar orbits of the spacecraft. We did not investigate this beyond initial tests, and this could be a future topic of research.

The presented local method is versatile: the constraint (or resolution of the model) can easily be varied regionally. In addition, the method requires in general fewer computational resources. This gives this localized method several advantages. With improved global correlations for our local solution, this method can be an alternative to a global approach.

Appendix A: Equations for Gravity Anomalies and Gravity Disturbances

In Section 2, we introduced the gravity anomaly. Its relationship to the disturbing potential T is given in Equation 3. Here, we provide additional equations that we used to compute the acceleration on a spacecraft from gravity anomalies. We also provide additional details on the equivalence between anomalies and global spherical harmonics.

First, in Figure A1 we clarify the relationship between the different points that are used to define the gravity anomaly as in Equation 1. The point P is at the geoid, and it has a projection Q on the reference surface along the normal n of the reference surface. Then, the gravity anomaly Δg is defined as the difference in

gravity at P and normal gravity at Q, $\Delta g = g_P - \gamma_Q$. In the spherical approximation this results in Equation 2 that relates the anomaly to the disturbing potential T (e.g., Heiskanen & Moritz, 1984; Sjöberg & Bagherbandi, 2017).

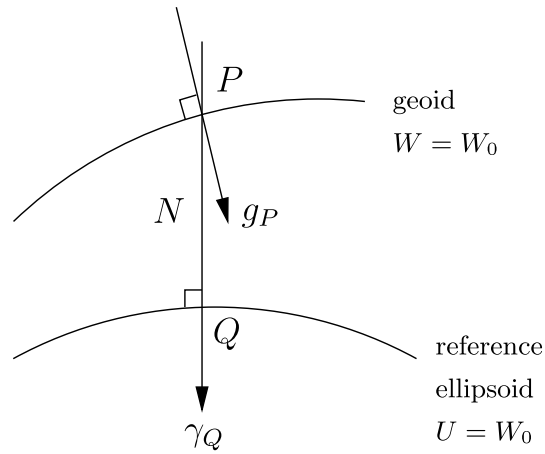

Figure A1. The geoid, the reference surface, and the points P and Q used in the definition of the gravity anomaly as given in Equation 1.

Conversely, the potential can also be expressed as a function of the anomalies. We repeat Equation 3 here for clarity:

$$T(P) = \frac{a_e}{4\pi} \iint_{\sigma(Q)} S(P,Q)\,\Delta g(Q)\,d\sigma(Q). \tag{A1}$$

The kernel in this expression, $S(P,Q)$, is called the Stokes-Pizetti kernel, where the point P is outside of the reference surface, which is the case when processing spacecraft data at altitude. This kernel is defined as (Heiskanen & Moritz, 1984):

$$S(r,\psi) = \frac{2a_e}{l(r,\psi)} + \frac{a_e}{r} - 3\frac{a_e\, l(r,\psi)}{r^2} - \frac{a_e^2}{r^2}\cos\psi\left(5 + 3\ln\frac{r - a_e\cos\psi + l(r,\psi)}{2r}\right), \tag{A2}$$

with

$$l(r,\psi) = \sqrt{r^2 + a_e^2 - 2\,r\,a_e\cos\psi} \tag{A3}$$

describing the distance between two points at distance r and a_e (the reference radius) from the center, separated by a spherical angle ψ. We also note that this kernel has a spectral equivalent, expressed in Legendre functions P_l (see also below):

$$S(r,\psi) = \sum_{l=2}^{\infty} \frac{2l+1}{l-1}\left(\frac{R}{r}\right)^{l+1} P_l(\cos\psi). \tag{A4}$$

This will allow a comparison between the anomaly expression for T and an expression in global spherical harmonics.

Because the integral in Equation A1 is over the entire surface, and the functions are harmonic outside of the Brillouin sphere (the circumscribing sphere that fits the entire mass of the body), spherical harmonic equivalents exist. First, we express the disturbing potential in spherical harmonics:

$$T(r,\lambda,\phi) = \frac{GM}{r}\sum_{l=0}^{\infty}\left(\frac{a_e}{r}\right)^l \sum_{m=0}^{l}\left(\bar{C}_{lm}\cos(m\lambda) + \bar{S}_{lm}\sin(m\lambda)\right)\bar{P}_{lm}(\sin\phi), \tag{A5}$$

where r, λ, ϕ are the spherical coordinates radius, longitude, and latitude, respectively, $\bar{C}_{lm}$ and $\bar{S}_{lm}$ are the normalized harmonic coefficients of the expansion of degree and order m, and $\bar{P}_{lm}$ are the normalized associated Legendre functions. Normalization here is the standard 4π normalization used in geodesy, which is given as:

$$\bar{P}_{lm}(\sin\phi) = \sqrt{(2-\delta_{0m})(2l+1)\frac{(l-m)!}{(l+m)!}}P_{lm}(\sin\phi), \tag{A6}$$

where δ_{0m} is the Kronecker delta which is 1 when $m = 0$ and 0 when $m \neq 0$. For normalization of the spherical harmonic coefficients $\bar{C}_{lm}$ and $\bar{S}_{lm}$ we note that $\bar{C}_{lm}\bar{P}_{lm} = C_{lm}P_{lm}$ (and the same for the S coefficients). Then, combining Equations 2 and A5 gives the spherical harmonics expression for the gravity anomaly, which we repeat here from Equation 4:

$$\Delta g(r,\lambda,\phi) = \frac{GM}{r^2}\sum_{l=2}^{\infty}(l-1)\left(\frac{a_e}{r}\right)^l\sum_{m=0}^{l}\left(\bar{C}_{lm}\cos(m\lambda)+\bar{S}_{lm}\sin(m\lambda)\right)\bar{P}_{lm}(\sin\phi). \tag{A7}$$

Equivalency of the expressions as given in Equations A1 and A5 can be shown by using the orthonormality relationships and addition theorem for (associated) Legendre functions.

For completeness, we also include expressions for the gravity disturbance $\delta g = -\partial T / \partial r$. In spherical harmonics, the disturbance can be expressed as:

$$\delta g(r,\lambda,\phi) = \frac{GM}{r^2}\sum_{l=2}^{\infty}(l+1)\left(\frac{a_e}{r}\right)^l\sum_{m=0}^{l}\left(\bar{C}_{lm}\cos(m\lambda)+\bar{S}_{lm}\sin(m\lambda)\right)\bar{P}_{lm}(\sin\phi). \tag{A8}$$

As indicated in Equation A7, the anomaly has a factor of $(l-1)$ in the spherical harmonics expression, and as can be seen from Equation A8, the disturbance has a factor of $(l+1)$. An expression similar to Equation A1 can also be found to express the potential as a function of the disturbance:

$$T(P) = \frac{a_e}{4\pi}\iint_{\sigma(Q)} H(r,\psi)\,\delta g(Q)\,d\sigma(Q), \tag{A9}$$

where the kernel has now become the Hotine kernel $H(r,\psi)$:

$$H(r,\psi) = \frac{2a_e}{l(r,\psi)} - \ln\left(\frac{l(r,\psi)+a_e-r\cos\psi}{r(1-\cos\psi)}\right). \tag{A10}$$

The next step is to compute accelerations on the spacecraft from the expression of the potential as given in Equation A1. The accelerations in three orthogonal directions (radial, denoted with δ_r, east-west, denoted with δ_λ, and north-south, denoted with δ_ϕ), can be obtained from:

$$\delta_r = \frac{\partial T}{\partial r};\ \delta_\phi = \frac{1}{r}\frac{\partial T}{\partial \phi};\ \delta_\lambda = \frac{1}{r\cos\phi}\frac{\partial T}{\partial \lambda}. \tag{A11}$$

Applying this to Equation A1 results in:

$$\delta_r(P) = \frac{a_e}{4\pi}\iint_{\sigma(Q)}\frac{\partial S(r,\psi)}{\partial r}\Delta g(Q)\,d\sigma(Q), \tag{A12}$$

$$\delta_\phi(P) = \frac{a_e}{4\pi r}\iint_{\sigma(Q)}\frac{\partial S(r,\psi)}{\partial \phi}\Delta g(Q)\,d\sigma(Q), \tag{A13}$$

$$\delta_\lambda(P) = \frac{a_e}{4\pi r\cos\phi}\iint_{\sigma(Q)}\frac{\partial S(r,\psi)}{\partial \lambda}\Delta g(Q)\,d\sigma(Q). \tag{A14}$$

The derivatives of the Stokes-Pizetti kernel with respect to r and ψ can be found from Equation A2:

$$\frac{\partial S(r,\psi)}{\partial r} = -\frac{a_e(r^2-a_e^2)}{rl^3} - \frac{4a_e}{rl} - \frac{a_e}{r^2} + \frac{6\,a_e\,l}{r^3} + \frac{a_e^2}{r^3}\cos\psi\left[13 + 6\ln\left(\frac{r - a_e\cos\psi + l}{2r}\right)\right], \tag{A15}$$

$$\frac{\partial S(r,\psi)}{\partial \psi} = \sin\psi\left[-\frac{2a_e^2 r}{l^3} - \frac{6a_e^2}{rl} + \frac{8a_e^2}{r^2} + \frac{3a_e^2}{r^2}\left(\frac{r - a_e\cos\psi - l}{l\sin^2\psi} + \ln\left(\frac{r - a_e\cos\psi + l}{2r}\right)\right)\right], \tag{A16}$$

where l is given by Equation A3. In order to express derivatives of the kernel with respect to the λ and ϕ directions, as required in Equations A12–A14, we use the definition of the angle ψ_{PQ} between two points $P(\lambda,\phi)$ and $Q(\lambda',\phi')$:

$$\cos\psi_{PQ} = \sin\phi\sin\phi' + \cos\phi\cos\phi'\cos(\lambda' - \lambda). \tag{A17}$$

Using the chain rule, the derivatives of $S(r,\psi)$ can be written as:

$$\begin{aligned}\frac{\partial S(r,\psi)}{\partial \phi} &= \frac{\partial S(r,\psi)}{\partial \psi}\frac{\partial \psi}{\partial \phi},\\ \frac{\partial S(r,\psi)}{\partial \lambda} &= \frac{\partial S(r,\psi)}{\partial \psi}\frac{\partial \psi}{\partial \lambda}.\end{aligned} \tag{A18}$$

With the definition of ψ as in Equation A17, the derivatives of ψ with respect to λ and ϕ can be obtained as:

$$\begin{aligned}-\sin\psi\frac{\partial \psi}{\partial \phi} &= \cos\phi\sin\phi' - \sin\phi\cos\phi'\cos(\lambda' - \lambda)\\ -\sin\psi\frac{\partial \psi}{\partial \lambda} &= \cos\phi\cos\phi'\sin(\lambda' - \lambda).\end{aligned} \tag{A19}$$

This set of equations allows the computation of the acceleration on the spacecraft through Equations A12–A14.

As stated in Section 2.2, we discretize the integral equations by replacing the integral with a sum over gridded gravity anomalies. The expression for the radial acceleration is given in Equation 7, and the expressions for the other directions are similar.

Data Availability Statement

The data used in this analysis can be found at the GRAIL archive on the PDS, https://pds-geosciences.wustl.edu/missions/grail/default.htm. In the directories, there one can find the KBRR data (https://pds-geosciences.wustl.edu), as well as auxiliary data, such as global gravity field models (https://pds-geosciences.wustl.edu). LOLA topography data such as spherical harmonic expansions of the topography we used here can be found at the LOLA PDS Data Node (http://imbrium.mit.edu). The results presented here are available for public use. Spherical harmonics models for gravity and Bouguer can be found at the PDS, as files labeled "gggrx_1200l" at the location for global models listed above. Additional products such as gridded anomalies are available from our data archive, at https://pgda.gsfc.nasa.gov/products/80. We used the freely available software SHTOOLS (Wieczorek et al., 2018) to compute localized correlations. All figures were made with the freely available software GMT (Wessel et al., 2013).

Acknowledgments
This work was supported by NASA grant NNX15AJ65G. We thank Dr. Anton Ermakov and an anonymous reviewer for their constructive comments. We are grateful for support from the NASA Center for Climate Simulation (NCCS) at NASA Goddard Space Flight Center. We used their supercomputer extensively for this work.

References

Anderson, J. D., Schubert, G., Jacobson, R. A., Lau, E. L., Moore, W. B., & Palguta, J. L. (2004). Discovery of mass anomalies on Ganymede. *Science*, *305*, 989–991. https://doi.org/10.1126/science.1099050

Asmar, S. W., Konopliv, A. S., Watkins, M. M., Williams, J. G., Park, R. S., Kruizinga, G., et al. (2013). The scientific measurement system of the Gravity Recovery and Interior Laboratory (GRAIL) mission. *Space Science Reviews*, *178*(1), 25–55. https://doi.org/10.1007/s11214-013-9962-0

Barriot, J.-P., Valès, N., Balmino, G., & Rosenblatt, P. (1998). A 180th degree and order model of the Venus gravity field from Magellan line of sight residual Doppler data. *Geophysical Research Letters*, *25*(19), 3743–3746. https://doi.org/10.1029/98GL02600

Besserer, J., Nimmo, F., Wieczorek, M. A., Weber, R. C., Kiefer, W. S., McGovern, P. J., et al. (2014). GRAIL gravity constraints on the vertical and lateral density structure of the lunar crust. *Geophysical Research Letters*, *41*, 5771–5777. https://doi.org/10.1002/2014GL060240

Beuthe, M., Rosenblatt, P., Dehant, V., Barriot, J.-P., Pätzold, M., Häusler, B., et al. (2006). Assessment of the Martian gravity field at short wavelength with Mars Express. *Geophysical Research Letters*, *33*, L03203. https://doi.org/10.1029/2005GL024317

Bills, B. G., & Ferrari, A. J. (1980). A harmonic analysis of lunar gravity. *Journal of Geophysical Research*, *85*(B2), 1013–1025. https://doi.org/10.1029/JB085iB02p01013

Chin, G., Brylow, S., Foote, M., Garvin, J., Kasper, J., Keller, J., et al. (2007). Lunar reconnaissance orbiter overview: The instrument suite and mission. *Space Science Reviews*, *129*, 391–419. https://doi.org/10.1007/s11214-007-9153-y

Crosby, A., & McKenzie, D. (2005). Measurements of the elastic thickness under ancient lunar terrain. *Icarus*, *173*, 100–107. https://doi.org/10.1016/j.icarus.2004.07.017

Deutsch, A. N., Neumann, G. A., Head, J. W., & Wilson, L. (2019). GRAIL-identified gravity anomalies in Oceanus Procellarum: Insight into subsurface impact and magmatic structures on the Moon. *Icarus*, *331*, 192–208. https://doi.org/10.1016/j.icarus.2019.05.027

Floberghagen, R. (2001). *The far side-lunar gravimetry into the third millennium* (Unpublished doctoral dissertation). Delft University of Technology. http://resolver.tudelft.nl/uuid:860293f4-1a66-4cf2-9cc9-1d2318a6709f

Floberghagen, R. (2002). *Lunar gravimetry* (Vol. 273). Dordrecht The Netherlands Kluwer Academic Publishers.

Goossens, S., Ishihara, Y., Matsumoto, K., & Sasaki, S. (2012). Local lunar gravity analysis over the South Pole-Aitken basin from SELENE farside tracking data. *Journal of Geophysical Research*, *117*, E02005. https://doi.org/10.1029/2011JE003831

Goossens, S., James, P. B., Mazarico, E., & Genova, A. (2019). Estimation of crust and lithospheric properties for mercury from high-resolution gravity field models. In *50th lunar and planetary science conference, The Woodlands, Texas, USA*. (Abstract 2202).

Goossens, S., Lemoine, F. G., Sabaka, T. J., Nicholas, J. B., Mazarico, E., Rowlands, D. D., & Zuber, M. T. (2016). A global degree and order 1200 model of the lunar gravity field using GRAIL mission data. In *47th lunar and planetary science conference, The Woodlands, Texas, USA*. (Abstract 1484).

Goossens, S., Matsumoto, K., Liu, Q., Kikuchi, F., Sato, K., Hanada, H., et al. (2011). Lunar gravity field determination using SELENE same-beam differential VLBI tracking data. *Journal of Geodesy*, *85*, 205–228. https://doi.org/10.1007/s00190-010-0430-2

Goossens, S., Mazarico, E., Genova, A., Lemoine, F. G., Neumann, G. A., Zuber, M. T., & Solomon, S. C. (2015). High-resolution gravity models for Mercury from MESSENGER tracking data. In *American geophysical union fall meeting* (Abstract P41C-2077).

Goossens, S., Sabaka, T. J., Nicholas, J. B., Lemoine, F. G., Rowlands, D. D., Mazarico, E., et al. (2014). High-resolution local gravity model of the south pole of the Moon from GRAIL extended mission data. *Geophysical Research Letters*, *41*, 3367–3374. https://doi.org/10.1002/2014GL060178

Goossens, S., Sabaka, T. J., Wieczorek, M. A., Neumann, G. A., Mazarico, E., Lemoine, F. G., et al. (2020). High-resolution gravity field models from grail data and implications for models of the density structure of the moon's crust. *Journal of Geophysical Research: Planets*, *125*, e2019JE006086. https://doi.org/10.1029/2019JE006086

Goossens, S., Visser, P. N. A. M., & Ambrosius, B. A. C. (2005). A method to determine regional lunar gravity fields from earth-based satellite tracking data. *Planetary and Space Science*, *53*, 1331–1340. https://doi.org/10.1016/j.pss.2005.06.009

Goossens, S., Visser, P. N. A. M., Heki, K., & Ambrosius, B. A. C. (2005). Local gravity from Lunar Prospector tracking data: Results for Mare Serenitatis. *Earth Planets and Space*, *57*(11), 1127–1132. https://doi.org/10.1186/BF03351893

Groetsch, C. (1993). *Inverse problems in the mathematical sciences*. Braunschweig/Wiesbaden Friedrich Vieweg & Sohn Verlagsgesellschaft.

Hackney, R., & Featherstone, W. (2003). Geodetic versus geophysical perspectives of the 'gravity anomaly'. *Geophysical Journal International*, *154*, 35–43. https://doi.org/10.1046/j.1365-246x.2003.01941.x

Han, S.-C. (2004). Efficient determination of global gravity field from satellite-to-satellite tracking mission. *Celestial Mechanics and Dynamical Astronomy*, *88*, 69–102. https://doi.org/10.1023/B:CELE.0000009383.07092.1f

Han, S.-C. (2008). Improved regional gravity fields on the Moon from Lunar Prospector tracking data by means of localized spherical harmonic functions. *Journal of Geophysical Research*, *113*, E11012. https://doi.org/10.1029/2008JE003166

Han, S.-C. (2013). Determination and localized analysis of intersatellite line of sight gravity difference: Results from the GRAIL primary mission. *Journal of Geophysical Research*, *118*, 2323–2337. https://doi.org/10.1002/2013JE004402

Han, S.-C., Mazarico, E., & Lemoine, F. G. (2009). Improved nearside gravity field of the Moon by localizing the power law constraint. *Geophysical Research Letters*, *36*, L11203. https://doi.org/10.1029/2009GL038556

Han, S.-C., Mazarico, E., Rowlands, D. D., Lemoine, F. G., & Goossens, S. (2011). New analysis of Lunar Prospector radio tracking data brings the nearside gravity field of the Moon with an unprecedented resolution. *Icarus*, *215*(2), 455–459. https://doi.org/10.1016/j.icarus.2011.07.020

Han, S.-C., Schmerr, N., Neumann, G., & Holmes, S. (2014). Global characteristics of porosity and density stratification within the lunar crust from GRAIL gravity and LOLA topography data. *Geophysical Research Letters*, *41*, 1882–1889. https://doi.org/10.1002/2014GL059378

Heiskanen, W. A., & Moritz, H. (1984). *Physical geodesy*. Graz, AustriaInstitute of physical geodesy (Original edition,1967. San Francisco. W. H. Freeman and Company).

Hirt, C., Featherstone, W. E., & Claessens, S. J. (2011). On the accurate numerical evaluation of geodetic convolution integrals. *Journal of Geodesy*, *85*, 519–538. https://doi.org/10.1007/s00190-011-0451-5

Kato, M., Sasaki, S., Takizawa, Y., & The Kaguya Project Team. (2010). The Kaguya mission overview. *Space Science Reviews*, *154*(1), 3–19. https://doi.org/10.1007/s11214-010-9678-3

Kaula, W. M. (1966). *Theory of satellite geodesy, applications of satellites to geodesy*. Waltham MA Blaisdell Publishing Company.

Kaula, W. M. (1996). Regional gravity fields on Venus from tracking of Magellan cycles 5 and 6. *Journal of Geophysical Research*, *101*(E2), 4683–4690. https://doi.org/10.1029/95JE02296

Kikuchi, F., Liu, Q., Hanada, H., Kawano, N., Matsumoto, K., Iwata, T., et al. (2009). Pico-second accuracy VLBI of the two sub-satellites of SELENE (KAGUYA) using multi-frequency and same-beam methods. *Radio Science*, *44*, RS2008. https://doi.org/10.1029/2008RS003997

Klipstein, W., Arnold, B., Enzer, D., Ruiz, A., Tien, J., Wang, R., & Dunn, C. (2013). The lunar gravity ranging system for the gravity recovery and interior laboratory (GRAIL) mission. *Space Science Reviews*, *178*(1), 57–76. https://doi.org/10.1007/s11214-013-9973-x

Konopliv, A. S., Asmar, S. W., Carranza, E., Sjogren, W. L., & Yuan, D. N. (2001). Recent gravity models as a result of the lunar prospector mission. *Icarus*, *150*, 1–18. https://doi.org/10.1006/icar.2000.6573

Konopliv, A. S., Banerdt, W. B., & Sjogren, W. L. (1999). Venus gravity: 180th degree and order model. *Icarus*, *139*, 3–18. https://doi.org/10.1006/icar.1999.6086

Konopliv, A. S., Park, R. S., Yuan, D.-N., Asmar, S. W., Watkins, M. M., Williams, J. G., et al. (2013). The JPL lunar gravity field to spherical harmonic degree 660 from the GRAIL Primary Mission. *Journal of Geophysical Research*, *118*, 1415–1434. https://doi.org/10.1002/jgre.20097

Konopliv, A. S., Park, R. S., Yuan, D.-N., Asmar, S. W., Watkins, M. M., Williams, J. G., et al. (2014). High-resolution lunar gravity fields from the GRAIL Primary and Extended Missions. *Geophysical Research Letters*, *41*, 1452–1458. https://doi.org/10.1002/2013GL059066

Kusche, J. (2003). Noise variance estimation and optimal weight determination for GOCE gravity recovery. *Advances in Geosciences*, *1*, 81–85. https://doi.org/10.5194/adgeo-1-81-2003

Lemoine, F. G., Goossens, S., Sabaka, T. J., Nicholas, J. B., Mazarico, E., Rowlands, D. D., et al. (2013). High-degree gravity models from GRAIL primary mission data. *Journal of Geophysical Research*, *118*, 1676–1698. https://doi.org/10.1002/jgre.20118

Lemoine, F. G., Goossens, S., Sabaka, T. J., Nicholas, J. B., Mazarico, E., Rowlands, D. D., et al. (2014). GRGM900C: A degree-900 lunar gravity model from GRAIL primary and extended mission data. *Geophysical Research Letters*, *41*, 3382–3389. https://doi.org/10.1002/2014GL060027

Lemoine, F. G. R., Smith, D. E., Zuber, M. T., Neumann, G. A., & Rowlands, D. D. (1997). A 70th degree lunar gravity model (GLGM-2) from Clementine and other tracking data. *Journal of Geophysical Research*, *102*(E7), 16339–16359. https://doi.org/10.1029/97JE01418

Li, X., & Götze, H.-J. (2001). Tutorial: Ellipsoid, geoid, gravity, geodesy and geophysics. *Geophysics*, *66*(6), 1660–1668. https://doi.org/10.1190/1.1487109

Liu, Q., Kikuchi, F., Matsumoto, K., Goossens, S., Hanada, H., Harada, Y., et al. (2010). Same-beam VLBI Observations of SELENE for Improving Lunar Gravity Field Model. *Radio Science*, *45*, RS2004. https://doi.org/10.1029/2009RS004203

Loomis, B. D., Luthcke, S. B., & Sabaka, T. J. (2019). Regularization and error characterization of GRACE mascons. *Journal of Geodesy*, *93*(9), 1381–1398. https://doi.org/10.1007/s00190-019-01252-y

Luthcke, S. B., Rowlands, D. D., Lemoine, F. G., Klosko, S. M., Chinn, D., & McCarthy, J. J. (2006). Monthly spherical harmonic gravity field solutions determined from GRACE inter-satellite range-rate data. *Geophysical Research Letters*, *33*, L02402. https://doi.org/10.1029/2005GL024846

Luthcke, S. B., Sabaka, T. J., Loomis, B. D., Arendt, A. A., McCarthy, J. J., & Camp, J. (2013). Antarctica, Greenland and Gulf of Alaska land-ice evolution from an iterated GRACE global mascon solution. *Journal of Glaciology*, *59*(216), 613–631. https://doi.org/10.3189/2013JoG12J147

Matsumoto, K., Goossens, S., Ishihara, Y., Liu, Q., Kikuchi, F., Iwata, T., et al. (2010). An improved lunar gravity field model from SELENE and historical tracking data: Revealing the farside gravity features. *Journal of Geophysical Research*, *115*, E06007. https://doi.org/10.1029/2009JE003499

Montenbruck, O., & Gill, E. (2000). *Satellite orbits*. Springer-Verlag.

Moritz, H. (1978). Least-squares collocation. *Reviews of Geophysics and Space Physics*, *16*(3), 421–430. https://doi.org/10.1029/RG016i003p00421

Muller, P., & Sjogren, W. (1968). Mascons: Lunar mass concentrations. *Science*, *161*, 680–684. https://doi.org/10.1126/science.161.3842.680

Namiki, N., Iwata, T., Matsumoto, K., Hanada, H., Noda, H., Goossens, S., et al. (2009). Farside gravity field of the moon from four-way doppler measurements of SELENE (Kaguya). *Science*, *323*, 900–905. https://doi.org/10.1126/science.1168029

Palguta, J., Anderson, J. D., Schubert, G., & Moore, W. B. (2006). Mass anomalies on Ganymede. *Icarus*, *180*(2), 428–441. https://doi.org/10.1016/j.icarus.2005.08.020

Park, R. S., Konopliv, A. S., Yuan, D.-N., Asmar, S. W., Watkins, M. M., Williams, J. G., & Zuber, M. T. (2015). A high-resolution spherical harmonic degree 1500 lunar gravity field from the GRAIL mission. In *American geophysical union fall meeting, San Francisco, California, USA* (Paper 67307, Abstract G41B-01).

Pavlis, D. E., & Nicholas, J. B. (2017). *GEODYN II System Description* (Vol. 1–5, contractor report). Greenbelt MD SGT Inc.

Rowlands, D. D., Luthcke, S. B., Klosko, S. M., Lemoine, F. G. R., Chinn, D. S., McCarthy, J. J., et al. (2005). Resolving mass flux at high spatial and temporal resolution using GRACE intersatellite measurements. *Geophysical Research Letters*, *32*, L04310. https://doi.org/10.1029/2004GL021908

Rowlands, D. D., Luthcke, S. B., McCarthy, J. J., Klosko, S. M., Chinn, D. S., Lemoine, F. G., et al. (2010). Global mass flux solutions from GRACE: A comparison of parameter estimation strategies—Mass concentrations versus Stokes coefficients. *Journal of Geophysical Research*, *115*, B01403. https://doi.org/10.1029/2009JB006546

Rowlands, D. D., Ray, R. D., Chinn, D. S., & Lemoine, F. G. (2002). Short-arc analysis of intersatellite tracking data in a gravity mapping mission. *Journal of Geodesy*, *76*, 307–316. https://doi.org/10.1007/s00190-002-0255-8

Sabaka, T. J., Rowlands, D. D., Luthcke, S. B., & Boy, J.-P. (2010). Improving global mass flux solutions from Gravity Recovery and Climate Experiment (GRACE) through forward modeling and continuous time correlation. *Journal of Geophysical Research*, *115*, B11403. https://doi.org/10.1029/2010JB007533

Seber, G. A. F., & Wild, C. J. (1989). *Nonlinear regression*. Hoboken, New Jersey: Wiley-Interscience.

Sjöberg, L. E., & Bagherbandi, M. (2017). *Gravity inversion and integration*.Cham Switzerland Springer International Publishing AG. https://doi.org/10.1007/978-3-319-50298-4

Smith, D. E., Zuber, M. T., Jackson, G. B., Cavanaugh, J. F., Neumann, G. A., Riris, H., et al. (2010a). The lunar orbiter laser altimeter investigation on the lunar reconnaissance orbiter mission. *Space Science Reviews*, *150*, 209–241. https://doi.org/10.1007/s11214-009-9512-y

Smith, D. E., Zuber, M. T., Neumann, G. A., Lemoine, F. G., Mazarico, E., Torrence, M. H., et al. (2010b). Initial observations from the Lunar Orbiter Laser Altimeter (LOLA). *Geophysical Research Letters*, *37*, L18204. https://doi.org/10.1029/2010GL043751

Smith, D. E., Zuber, M. T., Neumann, G. A., Mazarico, E., Lemoine, F. G., J. W. H., III, et al. (2016). Summary of the results from the Lunar Orbiter Laser Altimeter after seven years in orbit. *Icarus*, *283*, 70–91. https://doi.org/10.1016/j.icarus.2016.06.006

Šprlák, M., Han, S. C., & Featherstone, W. E. (2020). Integral inversion of GRAIL inter-satellite gravitational accelerations for regional recovery of the lunar gravitational field. *Advances in Space Research*, *65*(1), 630–649. https://doi.org/10.1016/j.asr.2019.10.015

Sugano, T., & Heki, K. (2004a). High resolution gravity anomaly map from the lunar prospector line-of-sight acceleration data. *Earth Planets and Space*, *56*, 81–86. https://doi.org/10.1186/BF03352492

Sugano, T., & Heki, K. (2004b). Isostasy of the Moon from high-resolution gravity and topography data: Implication for its thermal history. *Geophysical Research Letters*, *31*, L24703. https://doi.org/10.1024/2004GL022059

Tapley, B., Bettadpur, S., Ries, J., Thompson, P., & Watkins, M. (2004a). GRACE measurements of mass variability in the earth system. *Science*, *305*, 503–505. https://doi.org/10.1126/science.1099192

Tapley, B., Schutz, B., & Born, G. (2004b). *Statistical orbit determination*. Burlington MA Elsevier Academic Press.

Tregoning, P., Purcell, A. P., Allgeyer, S., McQueen, H., & McClusky, S. (2017). The role of range acceleration observations and regularisation in the estimation of sub-monthly temporal gravity fields from GRACE observations. In *AGU fall meeting abstracts* (Vol. 2017, p. G31B-0900).

Tscherning, C., & Rapp, R. (1974). *Closed covariance expressions for gravity anomalies, geoid undulations, and deflections of the vertical implied by anomaly degree variance models (Reports of the Department of Geodetic Science No. 208)*. Ohio State University.

Wessel, P., Smith, W. H. F., Scharroo, R., Luis, J., & Wobbe, F. (2013). Generic mapping tools: Improved version released. *EOS, Transactions American Geophysical Union*, *94*, 409–410. https://doi.org/10.1002/2013EO450001

Wieczorek, M. A. (2008). Constraints on the composition of the Martian south polar cap from gravity and topography. *Icarus*, *196*, 506–517. https://doi.org/10.1016/j.icarus.2007.10.026

Wieczorek, M. A. (2015). Gravity and topography of the terrestrial planets. In G. Schubert (Ed.), *Treatise on geophysics* (2nd ed., pp. 153–193). Elsevier. https://doi.org/10.1016/B978-0-444-53802-4.00169-X

Wieczorek, M. A., Meschede, M., Sales de Andrade, E., Oshchepkov, I., Xu, B., & Walker, A. (2018). *Shtools: Version 4.3*. Zenodo. https://doi.org/10.5281/zenodo.1346663

Wieczorek, M. A., Neumann, G. A., Nimmo, F., Kiefer, W. S., Taylor, G. J., Melosh, H. J., et al. (2013). The crust of the moon as seen by GRAIL. *Science*, *339*(6120), 671–675. https://doi.org/10.1126/science.1231530

Wieczorek, M. A., & Phillips, R. J. (1998). Potential anomalies on a sphere: Applications to the thickness of the lunar crust. *Journal of Geophysical Research*, *103*(E1), 1715–1724. https://doi.org/10.1029/97JE03136

Wieczorek, M. A., & Simons, F. J. (2005). Localized spectral analysis on the sphere. *Geophysical Journal International*, *162*, 655–675. https://doi.org/10.1111/j.1365-246X.2005.02687.x

Wieczorek, M. A., & Simons, F. J. (2007). Minimum-variance multitaper spectral estimation on the sphere. *Journal of Fourier Analysis and Applications*, *13*(6), 665–692. https://doi.org/10.1007/s00041-006-6904-1

Zuber, M. T., Smith, D. E., Lehman, D. H., Hoffman, T. L., Asmar, S. W., & Watkins, M. M. (2013a). Gravity recovery and interior laboratory (GRAIL): Mapping the lunar interior from crust to core. *Space Science Reviews*, *178*(1), 3–24. https://doi.org/10.1007/s11214-012-9952-7

Zuber, M. T., Smith, D. E., Neumann, G. A., Goossens, S., Andrews-Hanna, J. C., Head, J. W., et al. (2016). Gravity field of the orientale basin from the gravity recovery and interior laboratory mission. *Science*, *354*, 438–441. https://doi.org/10.1126/science.aag0519

Zuber, M. T., Smith, D. E., Watkins, M. M., Asmar, S. W., Konopliv, A. S., Lemoine, F. G., et al. (2013b). Gravity field of the moon from the gravity recovery and interior laboratory (GRAIL) mission. *Science*, *339*(6120), 668–671. https://doi.org/10.1126/science.1231507